



Optimising the turning performance of serial split-hull underwater vehicles[☆]

Vishakh S. Kumar^{1,*}, Prabhu Rajagopal²

Centre for Nondestructive Evaluation, Department of Mechanical Engineering, IIT Madras, Chennai 600036, India

ARTICLE INFO

Keywords:

AUV
Manoeuvrability
Turning modes
Lateral force

ABSTRACT

This paper discusses optimising the 2D turning performance of serial split-hull underwater vehicles with symmetric hulls. Compared to traditional single-hull solutions, their unique design makes them appealing for bathymetry. Analysis of the turning motion of such vehicles is a topic of tremendous research interest. During the turning motion of an underwater vehicle, the lateral forces demand both surge and sway thrusters to maintain the path without slipping. This impacts the vehicle operation, making it harder to control, and uses more power. The net lateral force and associated sway thrust requirements can be significantly reduced using a split-hull design, where the individual hulls can have different orientations. It is possible to eliminate the sway thruster and cover the circular path using a split-hull underwater vehicle. The existence of the optimal turning configuration is proved where the need for lateral thrust is minimal compared to the axial one. The effects of turning diameter, joint torque, and axial thrust are also considered when choosing the vehicle configuration for the specific operational requirement. Experiments are used to validate the outcomes of the modelling and simulation. The knowledge gained here will aid in developing and effectively operating similar vehicles.

1. Introduction

1.1. Split-hull underwater vehicles

Underwater vehicles are crucial elements of modern technology and are employed for various tasks, including intervention, bathymetry, and inspection. Today, different underwater vehicles, such as Autonomous Underwater Vehicles (AUVs) and Remotely Operated underwater Vehicles (ROVs), are available. AUVs are frequently used for autonomous bathymetry, a task that would otherwise require a lot of time and effort from human operators. Along with being more dependable, safe, and effective at gathering data than manual bathymetry, they come in various sizes and configurations. Most commercially used AUVs have a single, torpedo-shaped hull configuration. There have been many attempts to increase their functionality, which has led to the development of unconventional AUVs like concepts that resemble snakes and fish. Instead of having a rigid, single hull, these concepts emphasise the serial split-hull design, which increases manoeuvrability. Numerous researches have focused on the locomotion of such vehicles using undulatory/oscillatory movements. The Amphirobot (Crespi and Ijspeert, 2006), which was inspired by eels and uses undulatory motion to produce thrust and navigate, is one notable example. Zuo

and Wang developed an amphibious snake-like robot with serpentine motion (Zuo and Wang, 2008) and worked to gain maximum speed by adjusting the undulation amplitude and frequency. Despite having excellent manoeuvrability, the surge speed was limited to 0.1 m/s, highlighting a severe weakness of the bio-inspired locomotion. A torpedo vehicle called ldquo-HRF (Chen et al., 2008) was created by Chen and Xia in 2008 to mimic the surge, yaw and pitch motions of fish. Fish locomotion was thoroughly modelled by Yu and Wang, who also showed the ideal link length ratio for achieving the highest possible locomotion efficiency (Yu and Wang, 2007). Hirata modelled the turning motion of a vehicle with a fish-inspired design (Hirata et al., 2000), and the results showed how frequency, amplitude, and tail leaning affected the turning performance. According to the research conducted by Wiens and Nahon (2012), when a swimmer imitates the speed control mechanism of a fish, swimming efficiency dramatically increases because of the energy recovery processes. Kelasidi's group has studied underwater snake-like vehicles and modelled their locomotion very similar to the corresponding land-based vehicles (Kelasidi and Liljeback, 2016; Kelasidi, 2015). They discovered that, regardless of low surge speed, underwater snake-like robots are more energy-efficient than ROVs with traditional rotary thrusters in terms of transportation

[☆] This document is the results of the research project funded by the National Technology Centre for Ports, Waterways & Coasts, Indian Institute of Technology Madras, India.

* Corresponding author.

E-mail addresses: vishakhskumar1995@gmail.com (V.S. Kumar), prajagopal@iitm.ac.in (P. Rajagopal).

¹ Researcher.

² Co-ordinator.

costs (Kelasidi et al., 2015). In 2014, Liljeback and Stavdahl created a model of the snake-like robot named Mamba and investigated its motion. Although it was designed to be a land robot, Kelasidi modified it by mounting rotary thrusters on the rear side (Kelasidi et al., 2016) and carried out numerous experiments. The main goal was to overcome the limited agility of snake-like locomotion. The analysis revealed that using snake-like undulation for turning control and rotary thrusters for surge motion can enhance the locomotion capabilities. The underwater swimming manipulator known as Eelume (Liljeback and Mills, 2017), which has a serial-split hull design inspired by snakes and a thruster-based locomotion system, was created using this concept. The entire vehicle can function as a robotic arm for underwater inspection and maintenance tasks due to its distinctive design (Sverdrup-Thygeson and Kelasidi, 2017). The motion of underwater snake-like vehicles with rotary thrusters has received limited research. A few of them include the work by Sverdrup, who discovered the ideal force allocation matrix for an underwater snake-like vehicle that uses thrusters instead of body movements for locomotion (Sverdrup-Thygeson et al., 2016). An extended work by Borlaug et al. (2019) includes the modelling and control system design for the same vehicle that can be used for underwater manipulator operations. They also suggested a sliding mode control law for the trajectory tracking performance (Borlaug and Gravdahl, 2019). Amundsen used these works to show the in-depth analysis of the control system design of an underwater swimming manipulator vehicle that included reaction and hydrostatic force compensation. Hoffmann recently developed a path-following and collision-avoidance system (Hoffmann, 2018) for the same vehicle. These are a few notable studies on split/multi-hull underwater vehicles.

This paper discusses optimising the turning configuration of a serial split-hull underwater vehicle and is structured as follows. The importance of optimising the turning motion is discussed first, and then the simulation outcomes are presented, including the comparison of various hull configurations. This information determines the best turning configuration for the particular operational needs. It is followed with recommendations for future research after validating the findings with a prototype split-hull underwater vehicle.

1.2. Motivation for the split-hull design

There is much interest in developing a 2D bathymetry AUV to map water bodies with high manoeuvrability and operational efficiency. Low turning diameter and high manoeuvrability are made possible by a serial split-hull design with a modular hull configuration, as suggested by the authors (Kumar and Rajagopal, 2021, 2019). Additionally, this design makes it possible to add or remove hulls depending on the required payload, which is impossible with a traditional single-hull design. Also, the increase in turning diameter brought on by the extra modules is negligible. Rotary thrusters are used on the vehicle to resolve the low agility problems caused by the bio-inspired locomotion (Wiens and Nahon, 2012; Dharwada et al., 2018; Krishnadas et al., 2018; Dharwada et al., 2019). The cylinder-shaped hulls are joined in series by single-axis (Z) servo joints to enable precise yaw control. Fig. 1 illustrates the fundamental concept of improving the turning diameter using a split-hull vehicle. The CAD design of a three-hull configuration vehicle emphasising the thrusters and servo joints is shown in Fig. 2. During the development phase, it is discovered that the split-hull underwater vehicle requires some additional considerations that are unnecessary for a conventional one. They consist of the vehicle structural rigidity, which is essential during operation when the joints become critical zones. It will have an impact on the number of hulls for a specific vehicle length. It is identified by the hull configuration number (N) and is affected by several factors, including the thrust/joint torque capacity of the vehicle and the payload. Another crucial factor is the lateral thrust requirement for the turning/circular motion, which is present in any underwater vehicle. The vehicle must have pure surge (u) and yaw (ω) velocities with minimal sideways slip/sway (v)

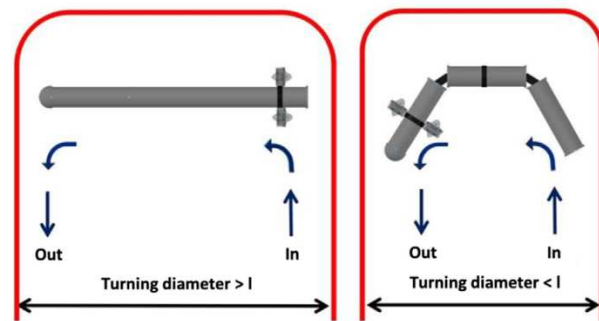


Fig. 1. Comparison of the space requirement while turning for a single hull AUV and a three-hull AUV with the same total length l .

during the turning motion for a robust mapping process. However, the Coriolis and centrifugal forces (Zhang et al., 2015) act laterally on the hull(s), necessitating the continuous use of sway and surge thrusters to keep the vehicle from slipping. One way to deal with this is to first come to a complete stop, after which the surge thrusters can produce the yaw through their differential action. While this method eliminates the need for a sway thruster, it is not ideal for bathymetry due to its lengthy operation time and inability to follow a circular path. With a split-hull design, the lateral forces act in a different direction depending on how each hull is oriented during the turning motion. It is possible to minimise or eliminate the net lateral force and the corresponding sway thrust requirement of the vehicle by selecting the appropriate joint angles (ϕ), which determine the turning mode (n). As a result, the circular path can be covered without using sway thrusters by just surge thrusters and servo joints. It is a significant advantage that split-hull underwater vehicles have over traditional ones. The lack of sway thrusters also simplifies the control system and lowers power consumption and in this way, introducing the concept of the “optimal turning mode” is very helpful. The optimal joint angle depends on the number, size, and shape of the hulls, which determine the vehicle configuration. It is important to note that a split-hull vehicle requires the combined action of both surge and sway thrusters for a non-optimal turning configuration. In such situations, failing to apply the sway thrust produces a net unbalanced force and causes slipping motion in the lateral direction. The turning configuration where the combined action of surge thrusters and the servo joints can facilitate the desired turning motion without a sway thruster has to be estimated for the specific vehicle configuration chosen. A few important factors must be considered to determine how the hull configuration (N) affects the turning performance. This includes the reduction in lateral thrust (f_{tN_y}), turning diameter ($2R$), and the joint torque requirement (τ_{ij}). The following section explains more specific details regarding the modelling assumptions.

To the authors' best knowledge, no prior literature has taken into account the detailed modelling and analysis of various modes of the turning motion of a split-hull underwater vehicle with rotary thrusters. With little prior research, analysis and optimisation of the turning motion of split-hull underwater vehicles contribute greatly as they draw more and more research attention. The difficulties encountered, as described in the motivation section, are relevant to developing any split-hull underwater vehicle. Therefore, the fundamental concept and the findings of this work will be beneficial and applicable for developing similar vehicles, and additional details about the design are discussed in the following section.

2. Methodology

2.1. Important aspects

The modelling employed in this paper is similar to that used for underwater snake-like vehicles, which has been shown to function well

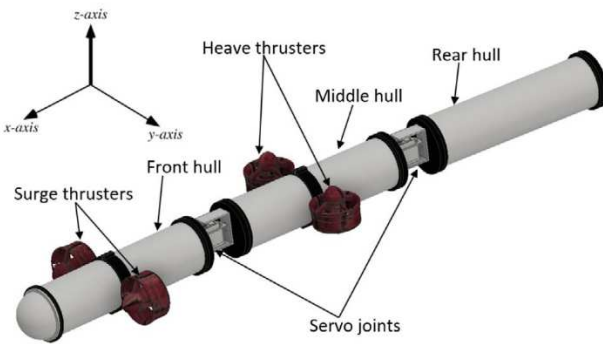


Fig. 2. CAD design showing the thrusters and servo joints in a three-hull configuration vehicle (M-Hull).

in the practical scenario (Kelasidi et al., 2017; Kelasidi and Liljeback, 2016; Sverdrup-Thygeson and Kelasidi, 2017). As long as the slender body theory holds true for each hull, the choice of the overall vehicle dimensions is irrelevant. The proposed vehicle's overall length is set at 3 metres because this is the typical length for most commercial AUVs (Allen et al., 1997; Prestero, 2001). Odd number hull configurations are chosen to have a symmetric vehicle structure and mount the heave thruster on the middle hull. As shown in Fig. 2, the middle hull has two heave thrusters on either side. This arrangement prevents undesirable pitch effects during heave motion because the driving forces act through the vehicle centre of gravity. The thrusters must be mounted on the hull joint section in the case of an even number hull configuration, which would be practically challenging. Due to the limited size of the hulls, fixing the heave thruster inside the hulls, as seen with some vehicles (Prestero, 2001; Cruz and Matos, 2008), is also impractical. Each hull is neutrally buoyant, and adding heave thrusters on the middle hull, and horizontal surge thrusters on the front hull increases the rolling inertia of the vehicle. When these factors are added to the low turning speed, the effects of rolling and pitching are insignificant and not discussed in this paper. Since the proposed bathymetry operates exclusively in the pure XY plane with no heave effects, the heave thruster does not need to be continuously operated to maintain the depth of operation. Also, the surge thrusters are not operated while using the heave thruster to prevent the coupling effect, which is beyond the scope of this paper. The gravity and buoyancy terms are disregarded because each hull is designed to have the centre of gravity coincide with the centre of buoyancy. Similar to this, the added mass cross-terms (Severholt, 2017) are not taken into account because of the slender body criteria and the symmetric hull shapes about the xz, yz, and xy planes. The individual hulls are connected in series by servo joints, and each joint centre coincides with the rotational axis of the connected hulls. It is crucial to emphasise the unique characteristics of the 1st and N th hulls. While all the other hulls are in contact with two joints, they are only in contact with one. Hence, the cylindrical portions of these hulls are made slightly longer so that all hulls have the same physical length ($2L$). The discontinuity at the joint sections must also be considered because their shapes differ from those of the hull. The joints between the hulls can be covered with a flexible cylindrical connecting material to solve this problem, but the prototype vehicle used for model validation does not have this feature. Thus the effect of the joint section is incorporated in the modelling to have conditions comparable to the experimental setup. For the fluid coefficient calculations given in the dynamic modelling section, a new term called the discontinuity factor (d_f) is introduced to achieve this. It is important to note that even when the joint section is considered, the mass distribution of each hull is balanced during the design stage.

There are a few more things to consider when determining the vehicle dimensions. For all hull configurations, the length considered is always greater than 2.5 times the diameter (Cox, 1970) to meet the

slender body criteria. The diameter must be as small as possible and similar to the thruster dimensions to reduce axial drag. The thruster used is Bluerobotics T100, with an outer diameter of 0.1 m. As a result, the same hull diameter ($D = 0.1$ m) is chosen while also making room for the required payload. Additionally, it is ensured that all hulls in any vehicle configuration have equal joint angles (ϕ) and lengths ($2L$). If the vehicle is divided into eleven pieces, each hull will be 0.27 m long, or 2.7 times its diameter. Anything with more than eleven hulls will cause the length to be further reduced, which will change the slender body criteria (Cox, 1970). Three hulls, each measuring one metre in length, are the lower bound for the number of hulls. Because of the even hull vehicle structure and excessive stress on the servo joints, the two hull configuration is ignored. Hence, a vehicle having an odd number of hulls (N) between three and eleven is considered in this paper. Each hull is connected by a servo-controlled joint designed to generate sufficient torque to maintain the joint angle. There are no external disturbances, such as the effects of waves or currents on the vehicle, and the fluid being considered is steady pure water. As a result, the vehicle will be subject to drag, Coriolis-centrifugal, and added mass forces. The individual hulls must be examined before calculating the net force and torque acting on the entire vehicle. The following section provides more explanation about this procedure.

2.2. Design procedure

The optimal turning mode that minimises lateral thrust for each hull configuration (N) must be identified. The entire vehicle is divided into several smaller hulls based on the hull configuration. The joint angle (ϕ) being used determines the selected turning mode (n). The joint angle is chosen so that, while turning, the vehicle is oriented in a polygonal configuration. A polygon with $2N$ sides is chosen for the N -hull vehicle configuration to have a good turning effect, and the corresponding joint angles are discovered, as shown below.

$$\phi_0 = 360/2N = 180/N \quad (1)$$

It is known as the base joint angle (ϕ_0), and Fig. 3(a) illustrates the schematic diagram of a vehicle with three hulls aligned in the hexagonal turning mode ($2N = 6$). It is essential to dynamically model the vehicle, which involves calculating the forces, torques, and required axial (f_{tN_x}) and lateral (f_{tN_y}) thrust values. The thrust ratio (α_{xy}), the ratio of the axial thrust and the lateral thrust as shown below, is a new parameter defined for a proper comparison.

$$\alpha_{xy} = f_{tN_x}/f_{tN_y} \quad (2)$$

The front (N th) hull coordinate system is used to define (f_{tN_x}) and (f_{tN_y}), and the corresponding calculation is explained in the next section. By changing the turning mode, each hull configuration is further examined to determine how effectively it minimises the lateral thrust and to obtain this, a range of joint angles from $(\phi_0 - \Delta\phi)$ to $(\phi_0 + \Delta\phi)$ is selected. This range should include the optimal joint angle at which the maximum thrust ratio (α_{xy}) will appear; in this case, the considered range variation ($\Delta\phi$) is 12.5° . The parameters mentioned above are calculated for each turning mode, and the process is repeated for all odd number hull configurations (N) from three to eleven. Another parameter called Equivalent turning mode (n_{eq}) is provided below for ease of understanding.

$$n_{eq} = (\phi - \phi_0)/\Delta\phi \quad (3)$$

It shows the fractional deviation of the joint angle from the base value (ϕ_0). The turning mode with the lowest lateral thrust requirement or the highest thrust ratio (α_{xy}) is chosen as the optimal one for each hull configuration. Additionally, the turning diameter and joint torque requirement for each configuration must be considered. In short, the optimisation problem seeks to find the turning configuration with minimum turning diameter ($2R$), minimum joint torque requirement (τ_{ij}), and maximum thrust ratio (α_{xy}).

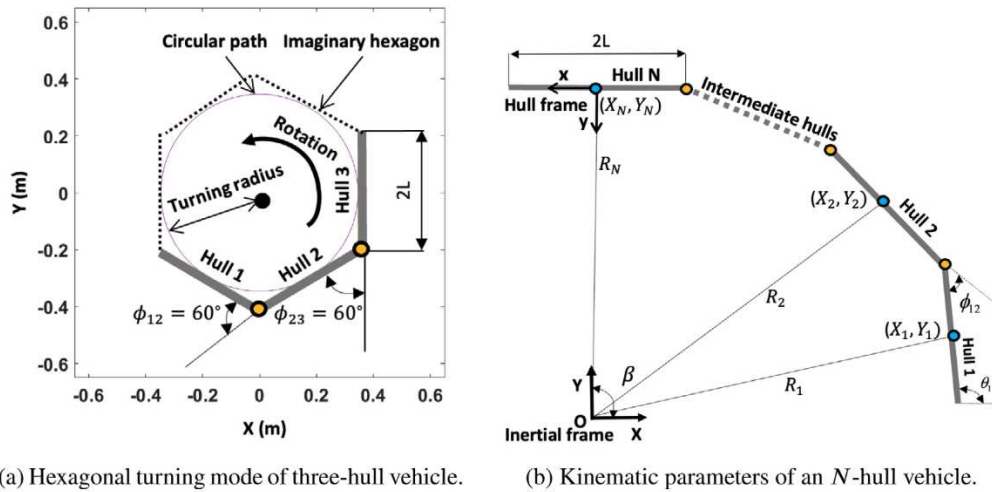


Fig. 3. Schematic diagram showing the hexagonal turning configuration for the three-hull vehicle and the general multi-hull kinematic parameters.

3. Synthesis of the vehicle model

The vehicle has to be modelled in a sufficiently simple manner while considering all the hydrodynamic effects to reduce the complexity of the control system. There are three analytical models suitable for underwater vehicles, all of which are based on the fluid mechanics theory of slender bodies (Kelasidi, 2015; Keller and Rubinow, 1976). The biomechanics community recommends the first one, and it is based on the Large Amplitude Elongated Body Theory (LAEBT) (Lighthill, 1971). The oceanic engineering community offers the second one to conduct the dynamic analysis of underwater flexible cables (Boyer et al., 2006). The third one is based on Morison's equation (Morison et al., 1950), and it is commonly used in the robotics community. The third model is followed here to calculate the forces between the fluid and the split-hull vehicle. There are many studies conducted based on this model on similar underwater vehicles (Kelasidi and Liljeback, 2016; Kelasidi, 2015; Sverdrup-Thygeson and Kelasidi, 2017), and they have been experimentally verified with sufficient accuracy. Although this paper concentrates more on the simulation results, the model validity is ensured through experiments at the end using a split-hull underwater vehicle. Note that the goals include proving the existence of the optimal turning mode, choosing the hull configuration that favours the highest thrust ratio (α_{xy}) and finding the penalty for not choosing the optimal turning mode. Hence, the analysis is started with the kinematic modelling of the vehicle. This step is essential for the dynamic modelling, where the hydrodynamic forces and torques acting on the vehicle are calculated. Then, the thrust ratio (α_{xy}) and other optimisation parameters are determined to compare the results for choosing the optimal hull configuration. The important parameters used for the analysis are explained in Table 1.

3.1. Kinematic modelling

The hull centres are used as the origin for the local coordinates, and the hulls are considered as links for this multi-body analysis. The global/inertial coordinates (XY) are fixed at the centre of the circular path, and the individual hull coordinate positions are related using the generalised kinematic equations given in Eqs. (4)–(11). The transformation matrix used for all the calculations is given in Eq. (12) along with all these details for the N -hull configuration vehicle in Fig. 3(b). To make the multi-body calculations simple, the following helpful matrices are used: The difference operator (D_o) and the addition operator (A_o) as depicted in Eqs. (21) and (22), respectively. There will be no tangential acceleration in a circular motion with constant angular velocity (ω), but there will be centripetal acceleration; more on this will be covered in

Table 1
List of parameters used for the dynamic analysis.

Symbol	Meaning
θ_i	Orientation of i th hull with respect to X axis (rad)
ϕ_{ij}	Joint angle between i th and j th hulls (rad)
m_i	Mass of i th hull (kg)
m_{TB}	Net buoyancy on the thruster (kg)
$2L$	Length of each hull (m)
a, b	Major and minor axis lengths of the elliptical cross section (m)
r	Radius of each hull ($D/2$) = 0.05 m
R	Radius of the curvature of path (m)
ρ	Density of water (1000 kg/m ³)
β	Turning angle used for the simulation (rad)
ω	Angular velocity of turning (rad/s)
v_r	Relative velocity in the hull frame (m/s)
c_{ii}	Axial drag coefficient for the i th hull (kg/m)
c_{nl}	Lateral drag coefficient for the i th hull (kg/m)
μ_{nl}	Lateral added mass coefficient for the i th hull (kg)
$h_{(i,j)}$	Joint constraint force between i th and j th hulls (N)
f_{el}	Net fluid force on the i th hull expressed in hull coordinates (N)
τ_{fi}	Fluid torque acting on the i th hull (N m)
$\tau_{(i,j)}$	Joint torque requirement at the i th joint (N m)
f_{INx}	Axial thrust requirement on the leading (N th) hull (N)
f_{INy}	Lateral thrust requirement on the leading (N th) hull (N)

the dynamic modelling section. The X and Y components of velocity and acceleration change due to the vehicle orientation. The kinematic constraint equations are provided below.

$$\begin{bmatrix} X_1 \\ Y_1 \end{bmatrix} + T_1 \begin{bmatrix} L \\ 0 \end{bmatrix} - \begin{bmatrix} X_2 \\ Y_2 \end{bmatrix} - T_2 \begin{bmatrix} -L \\ 0 \end{bmatrix} = 0 \quad (4)$$

$$\theta_2 - \theta_1 - \phi_{12} = 0 \quad (5)$$

$$\begin{bmatrix} X_2 \\ Y_2 \end{bmatrix} + T_2 \begin{bmatrix} L \\ 0 \end{bmatrix} - \begin{bmatrix} X_3 \\ Y_3 \end{bmatrix} - T_3 \begin{bmatrix} -L \\ 0 \end{bmatrix} = 0 \quad (6)$$

$$\theta_3 - \theta_2 - \phi_{23} = 0 \quad (7)$$

The same can be done with the remaining hulls. The constraint equations for the final hull are provided below in a similar way.

$$\begin{bmatrix} X_{N-1} \\ Y_{N-1} \end{bmatrix} + T_{N-1} \begin{bmatrix} L \\ 0 \end{bmatrix} - \begin{bmatrix} X_N \\ Y_N \end{bmatrix} - T_N \begin{bmatrix} -L \\ 0 \end{bmatrix} = 0 \quad (8)$$

$$\theta_N - \theta_{N-1} - \phi_{(N-1)(N)} = 0 \quad (9)$$

$$\begin{bmatrix} X_N \\ Y_N \end{bmatrix} - \begin{bmatrix} R \cos(\beta) \\ R \sin(\beta) \end{bmatrix} = 0 \quad (10)$$

$$\theta_N - \pi/2 = \beta \quad (11)$$

$$T_i = \begin{bmatrix} \cos(\theta_i) & -\sin(\theta_i) \\ \sin(\theta_i) & \cos(\theta_i) \end{bmatrix} \quad (12)$$

$$R = L/\tan(\phi/2). \quad (13)$$

Note that β is the angular position of the N th hull, which will be used for the simulation, and that the radius of the path (R) is taken as the radius of the incircle (Miles, 1964) corresponding to the hull configuration (N). Fig. 3(b) depicts the circle within which a three-hull configuration vehicle follows an imaginary hexagonal turning mode with a side length equal to the length of each hull ($2L$). The joint angle (ϕ_{ij}) is set at 60° to obtain the hexagonal shape as per Eq. (1). The joint angle used and the outer angle of the polygon under consideration are the same, as seen in Fig. 3(a). The vehicle appears to be rotating in the shape of a semi-hexagon as it follows the circular path. Note that the shape of the imaginary polygon changes with the joint angle, but the vehicle will still follow a circular path with a different radius. For the purpose of the kinematic modelling, the overall constraint matrix C is defined as shown in Eq. (14), where the individual elements $C_i, i \in [1, 3N]$ are the left-hand sides of the equations given in Eqs. (4)–(11). The right-hand side matrix β_1 has all terms equal to zero except the last term (β) corresponding to Eq. (11). The position matrix (X_t) can be obtained by solving Eq. (14) after substituting the value of β , which varies from 0 to 2π rad during the simulation. Eq. (15) gives the velocity characteristics of the vehicle using the time derivative of C .

$$C = \beta_1 \in \mathbb{R}^{3N \times 1} \quad (14)$$

$$\frac{\partial C}{\partial t} = \frac{\partial C}{\partial X_t} \frac{\partial X_t}{\partial t} = J_C \dot{X}_t = \dot{\beta}_1 \quad (15)$$

$$X_t = [X_1 \ Y_1 \ \theta_1 \ X_2 \ Y_2 \ \theta_2 \ \dots \ X_N \ Y_N \ \theta_N]^T \in \mathbb{R}^{3N \times 1} \quad (16)$$

Note that J_C is the Jacobian matrix of the constraint equations, which is calculated as

$$J_{C_{ij}} = \frac{\partial C_i}{\partial X_{tj}}, \quad i, j \in [1, 3N], \quad J_C \in \mathbb{R}^{3N \times 3N}. \quad (17)$$

Substituting $\dot{\beta} = \omega$ which is the angular velocity of the vehicle in Eq. (15) will give the values of the velocity matrix (\dot{X}_t) at any turning angle β . Differentiating Eq. (15) with time gives the acceleration characteristics of the vehicle as given in Eq. (18). Using the velocity values obtained before and then by substituting $\ddot{\beta} = 0$ due to the absence of angular acceleration in Eq. (18) will give the values of the corresponding acceleration matrix (\ddot{X}_t) shown below.

$$\frac{\partial^2 C}{\partial t^2} = J_J \dot{X}_t + J_C \ddot{X}_t = 0 \quad (18)$$

The new term J_J is the Jacobian of the constraint matrix Jacobian (J_C) for which i th column (J_{Ji}) is obtained as

$$J_{Ji} = \frac{\partial J_{Ci}}{\partial X_t} \dot{X}_t, \quad i \in [1, 3N], \quad J_J \in \mathbb{R}^{3N \times 3N}. \quad (19)$$

Note that Eq. (18) is a matrix multiplication where the first term $(\partial J_{Ci}/\partial X_t)$ has an order of $(3N \times 3N)$ and J_{Ci} is the i th column of J_C . This is the algorithm used for the simulation to determine the kinematic parameters for each hull at any point during the turning motion (β). The position constraint equations given in Eqs. (4)–(11) can be written in the multi-body form as Eq. (20), followed by all the matrices used for the multi-body analysis.

$$D_o X + A_o L \cos(\theta) = 0, \quad D_o Y + A_o L \sin(\theta) = 0 \quad (20)$$

where,

$$D_o = \begin{bmatrix} 1 & -1 & 0 & 0 & 0 & 0 & \dots & 0 \\ 0 & 1 & -1 & 0 & 0 & 0 & \dots & 0 \\ \cdot & \cdot \\ \cdot & \cdot \\ 0 & 0 & 0 & 0 & \cdot & \cdot & 1 & -1 \end{bmatrix} \in \mathbb{R}^{(N-1) \times N} \quad (21)$$

$$A_o = \begin{bmatrix} 1 & 1 & 0 & 0 & 0 & 0 & \dots & 0 \\ 0 & 1 & 1 & 0 & 0 & 0 & \dots & 0 \\ \cdot & \cdot \\ \cdot & \cdot \\ 0 & 0 & 0 & 0 & \cdot & \cdot & 1 & 1 \end{bmatrix} \in \mathbb{R}^{(N-1) \times N} \quad (22)$$

$$e = [1 \ 1 \ 1 \ \dots \ 1]^T, \quad \theta = [\theta_1 \ \theta_2 \ \dots \ \theta_N]^T \in \mathbb{R}^{N \times 1} \quad (23)$$

$$M = \text{diag}([m_1 \ m_2 \ \dots \ m_N]) \in \mathbb{R}^{N \times N} \quad (24)$$

$$L = \text{diag}([L_1 \ L_2 \ \dots \ L_N]) \in \mathbb{R}^{N \times N} \quad (25)$$

$$X = [X_1 \ X_2 \ \dots \ X_N]^T, \quad Y = [Y_1 \ Y_2 \ \dots \ Y_N]^T \in \mathbb{R}^{N \times 1} \quad (26)$$

$$\sin(\theta) = [\sin(\theta_1) \ \sin(\theta_2) \ \dots \ \sin(\theta_N)]^T \in \mathbb{R}^{N \times 1} \quad (27)$$

$$\cos(\theta) = [\cos(\theta_1) \ \cos(\theta_2) \ \dots \ \cos(\theta_N)]^T \in \mathbb{R}^{N \times 1} \quad (28)$$

$$S_\theta = \text{diag}([\sin(\theta_1) \ \sin(\theta_2) \ \dots \ \sin(\theta_N)]) \in \mathbb{R}^{N \times N} \quad (29)$$

$$C_\theta = \text{diag}([\cos(\theta_1) \ \cos(\theta_2) \ \dots \ \cos(\theta_N)]) \in \mathbb{R}^{N \times N} \quad (30)$$

$$c_t = \text{diag}([c_{t1} \ \dots \ c_{tN}]), \quad c_n = \text{diag}([c_{n1} \ \dots \ c_{nN}]) \in \mathbb{R}^{N \times N} \quad (31)$$

$$\mu_n = \text{diag}([\mu_{n1} \ \mu_{n2} \ \dots \ \mu_{nN}]) \in \mathbb{R}^{N \times N} \quad (32)$$

$$T = \begin{bmatrix} C_\theta & -S_\theta \\ S_\theta & C_\theta \end{bmatrix} \in \mathbb{R}^{2N \times 2N} \quad (33)$$

T is the combined coordinate transformation matrix and the position of the centre of gravity of the vehicle in the global coordinates is given by Eq. (34) where m_t is the total mass of the vehicle.

$$P_{CM} = \begin{bmatrix} P_X \\ P_Y \end{bmatrix} = \begin{bmatrix} \frac{1}{m_t} \sum_1^N m_i X_i \\ \frac{1}{m_t} \sum_1^N m_i Y_i \end{bmatrix} = \frac{1}{m_t} \begin{bmatrix} e^T M X \\ e^T M Y \end{bmatrix} \quad (34)$$

Using Eqs. (20) and (34), the relative configuration of individual hulls can be cross-verified whenever needed. Total mass of each hull has to meet the neutral buoyancy condition and hence mass of all hulls except the N th and middle hulls is given by

$$m_i = \frac{\pi}{4} D^2 (2L) \rho, \quad i \in [1, N-1], \quad i \neq (N+1)/2. \quad (35)$$

Total mass of the N th and middle hulls is different due to the presence of thrusters and it is given by Eq. (36) where m_{TB} is the net buoyancy on each thruster which is obtained from its specification.

$$m_N = m_{mid} = \frac{\pi}{4} D^2 (2L) \rho + 2m_{TB} \quad (36)$$

3.2. Dynamic modelling

The dynamic model must consider all external fluid forces that are important for the vehicle control system design. The external fluid forces acting include drag force (F_D) and added mass force (F_A). In all configurations, each hull is a slender body (Keller and Rubinow, 1976) with a length greater than 2.7 times the diameter, so Morison's equation (Morison et al., 1950) can be used to calculate the fluid forces. Due to the neutrally buoyant design, the net force for each hull in the Z direction is zero as the forces of gravity and buoyancy will cancel out. However, because the path is circular, the Coriolis and centrifugal force effects must be considered; as a result, it is used in calculating the total force. Eq. (39) is used to calculate the instantaneous hydrodynamic forces using the velocity and acceleration values obtained from the kinematic modelling. To calculate the net external force acting on the vehicle as given in Eq. (44), the fluid forces acting on the individual

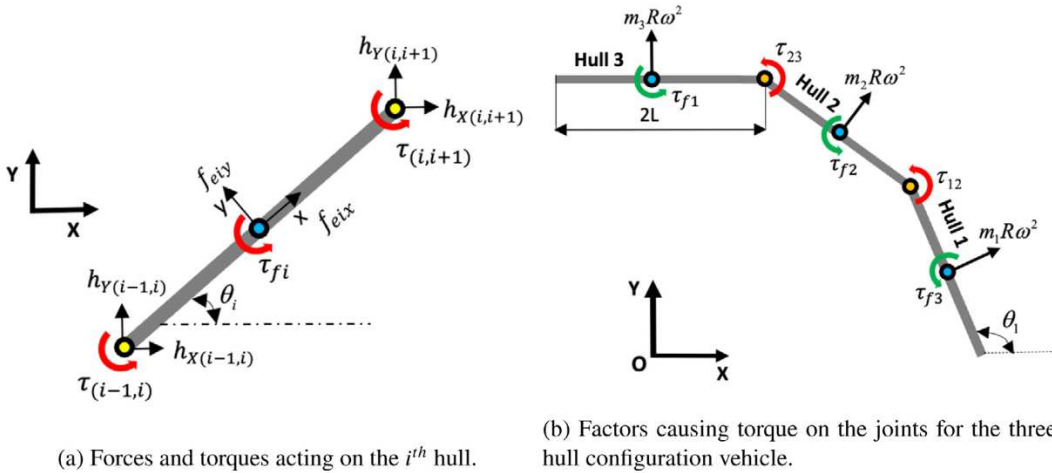


Fig. 4. Schematic depiction of the forces and torques acting on the vehicle.

hulls are estimated first. These forces are then added together in the global coordinates to calculate the net thrust requirement. There will be both x (axial) and y (lateral) components of the thrust when the values are transformed into the local coordinates, as shown in Eq. (52). Take note that the surge thrusters are situated only on the front hull (N th). When this lateral thrust component is unbalanced, the vehicle slips and more details about this are given at the end of this section.

3.2.1. Modelling the forces and thrust requirement

This section describes modelling the forces acting on the individual hulls and estimating the net thrust requirement. The drag and added mass forces for a general hull with an elliptical cross-section are expressed first. The ellipse is represented by the length of the semi-major axis (a) and semi-minor axis (b). In this case, the cylindrical hull will be a specific elliptical hull with $a = b = r$. The parameters must be modified to account for the effect of thrusters, as in the case of the front and middle hulls. The parameters for the front hull, which is equipped with the surge thrusters, are given by

$$a = (2r + d_t(h_t/2L))/2, \quad b = r. \quad (37)$$

Here, $d_t = 0.1$ m is the diameter and $h_t = 0.056$ m is the height of the thruster. In the case of the middle hull where heave thrusters are attached, the parameters are given by

$$a = (2r + d_t(d_t/2L))/2, \quad b = r. \quad (38)$$

Note that $a = b = r$ for the remaining hulls and the total external force on the i th hull is calculated in the global coordinates as the sum of added mass force (F_{Ai}) and drag force (F_{Di}) as follows.

$$F_{ei} = F_{Ai} + F_{Di} \quad (39)$$

The added mass force for the i th hull (F_{Ai}) is obtained by transforming the same from the hull coordinates (f_{Ai}) into the global/inertial coordinates as per Eq. (40) where C_A is the added mass coefficient matrix. Note that \dot{v}_{ri} is the relative acceleration matrix of the hull defined along the hull coordinates, and it is given below.

$$F_{Ai} = T_i f_{Ai} = -T_i C_{Ai} \dot{v}_{ri} \quad (40)$$

$$\dot{v}_{ri} = [\dot{v}_{rx} \quad \dot{v}_{ry}]^T, \quad C_{Ai} = \begin{bmatrix} 0 & 0 \\ 0 & \mu_{ni} \end{bmatrix} = \begin{bmatrix} 0 & 0 \\ 0 & \rho\pi C_a a^2 L_e \end{bmatrix} \quad (41)$$

L_e is the effective length given to each hull that includes the effect of thrusters. It is equal to $2L + 2h_t$ for the front hull, $2L + 2d_t/3$ for the middle hull and $2L$ for the remaining hulls. As the vehicle is turning at a constant speed, $\dot{v}_{rx} = 0$, but $\dot{v}_{ry} = R\omega^2$ due to the centripetal acceleration, and it results in the added mass force in the y -direction.

This component of added mass is a speciality of the rotational motion as it acts even though the hull has zero tangential acceleration. This is an interesting effect, and it is also known as the centripetal acceleration reaction force (Zhang et al., 2015). C_a is the lateral drag coefficient, and it depends on the type of flow, size and shape of the body and it will be explained at the end of this section. Note that the added mass force in the x -direction is negligible because it is much smaller in relation to the total mass for a slender body (Newman and Grue, 1977). The drag force F_{Di} is given below and it is taken as a function of both first and second orders of the relative velocity of the hull (v_{ri}) defined in the hull frame.

$$F_{Di} = T_i f_{Di} = -T_i (C_{Di} v_{ri} + C_{Dii} v_{ri} |v_{ri}|) \quad (42)$$

C_{Di} is the drag coefficient matrix for the i th hull which is given by

$$C_{Di} = \begin{bmatrix} c_{ii} & 0 \\ 0 & c_{ni} \end{bmatrix} = \begin{bmatrix} \frac{1}{2} \rho \pi C_f \frac{(a+b)}{2} L_e & 0 \\ 0 & \frac{1}{2} \rho C_d (2a) L_e \end{bmatrix}. \quad (43)$$

The total external force on the i th hull (F_{ei}) is the sum of the corresponding added mass and drag force terms ($F_{Ai} + F_{Di}$), and its components are shown in Fig. 4(a). The internal forces between the hulls (h_X, h_Y) shown in the same figure are not required for the analysis and hence are not discussed in this paper. As stagnant water is considered, the relative velocity is equal to the vehicle velocity itself and C_f is the drag coefficient along the x -direction and C_d is the drag coefficient along the y -direction. The relative velocity matrix in i th hull frame is given by $v_{ri} = [v_{rx} \quad v_{ry}]^T$. Due to the no-slip condition, v_{ryi} will be zero for all the hulls. The individual hull external force matrices are clubbed together to get the multi-body external force matrix, as shown below.

$$F_e = F_D + F_A \in \mathbb{R}^{2N \times 1} \quad (44)$$

$F_D \in \mathbb{R}^{2N \times 1}$ is the total drag matrix and $F_A \in \mathbb{R}^{2N \times 1}$ is the total added mass matrix. The first N terms in each matrix consist of the X component forces, and the remaining terms include the Y component forces corresponding to each hull. The forces can be calculated on individual hulls separately as per Eqs. (40) and (42) and then club them together to get the total external force matrix given in Eq. (44), but it gets complicated when the number of hulls is higher. Hence, the multi-body matrices given in Eqs. (21)–(33) are used to simplify the calculation from now onwards (Sverdrup-Thygeson et al., 2016).

$$F_D = - \begin{bmatrix} c_i C_0 & -c_i S_0 \\ c_i S_0 & c_i C_0 \end{bmatrix} \left(\begin{bmatrix} v_{rx} \\ v_{ry} \end{bmatrix} + \begin{bmatrix} \text{sign}(v_{rx}) v_{rx}^2 \\ \text{sign}(v_{ry}) v_{ry}^2 \end{bmatrix} \right) \quad (45)$$

$$F_A = - \begin{bmatrix} \mu_n S_0^2 & -\mu_n S_0 C_0 \\ -\mu_n S_0 C_0 & \mu_n C_0^2 \end{bmatrix} \begin{bmatrix} \dot{X} \\ \dot{Y} \end{bmatrix} \quad (46)$$

The terms v_{rx} and $v_{ry} \in \mathbb{R}^{N \times 1}$ are the combined surge and sway velocity matrices expressed in the hull coordinates and they can be obtained by transforming the global velocity values from Eq. (15) as

$$\begin{bmatrix} v_{rx} \\ v_{ry} \end{bmatrix} = T^T \begin{bmatrix} \dot{X} \\ \dot{Y} \end{bmatrix} \in \mathbb{R}^{2N \times 1}. \quad (47)$$

Here, only the first N terms will be non-zero due to the no-slip condition, and the overall dynamics of the entire vehicle can be expressed in the global coordinates as

$$M\ddot{X} = F_{tX} + F_{eX}, \quad M\ddot{Y} = F_{tY} + F_{eY} \in \mathbb{R}^{N \times 1}. \quad (48)$$

The terms F_{eX} and F_{eY} are respectively the first and second halves of the external force matrix given in Eq. (44). The global thrust matrices given by F_{tX} and F_{tY} are expressed as

$$\begin{bmatrix} F_{tX} \\ F_{tY} \end{bmatrix} = Tf_i \in \mathbb{R}^{2N \times 1} \quad (49)$$

$$f_t = [f_{t1x} \ f_{t2x} \ \dots \ f_{tNx} \ f_{t1y} \ f_{t2y} \ \dots \ f_{tNy}]^T \in \mathbb{R}^{2N \times 1}. \quad (50)$$

Note that f_t is the thrust force matrix in the hull coordinates where f_{tix} and f_{tiy} are respectively the surge (axial) and sway (lateral) thrust for the i th hull. For the proposed vehicle, the individual hulls do not have thrusters in the XY plane except for the N th hull. It means all the terms in Eq. (50) other than the one corresponding to the N th hull will be zero. The net force required to achieve the desired circular motion for each hull is obtained by summing up the inertia ($M\ddot{X}, M\ddot{Y}$) and the external (F_{eX}, F_{eY}) forces. The thrusters on the N th hull have to support all these forces, and hence it is calculated as the sum of individual hull force requirements in X and Y directions separately as follows.

$$f_{tNX} = e^T(M\ddot{X} - F_{eX}), \quad f_{tNY} = e^T(M\ddot{Y} - F_{eY}) \quad (51)$$

The thrust value obtained in the global coordinates is transformed into hull coordinates to obtain the required axial (f_{tNX}) and lateral (f_{tNY}) components, as shown below. The values of thrust requirement are calculated from Eq. (52), and the thrust ratio is obtained from Eq. (2), which will be discussed in detail in the results section.

$$\begin{bmatrix} f_{tNX} \\ f_{tNY} \end{bmatrix} = T_N^T \begin{bmatrix} f_{tNX} \\ f_{tNY} \end{bmatrix} \in \mathbb{R}^{2 \times 1} \quad (52)$$

3.2.2. Modelling the joint torque requirement

The estimation of the joint torque requirements is crucial for the turning motion analysis. This torque is required to balance out two components: One due to the external normal fluid force (τ_{fi}) on the hull, which is explained below, and the other due to the centrifugal force ($m_i R\omega^2$) on each hull. The method used in Kelasidi (2015), where the model of an underwater snake-like vehicle with general elliptical cross-sectional hulls was experimentally validated, is used here. The fluid torque action on the i th hull during the turning motion due to the change in orientation is given by

$$\tau_{fi} = -(\lambda_1 \ddot{\theta}_i + \lambda_2 \dot{\theta}_i + \lambda_3 \dot{\theta}_i |\dot{\theta}_i|). \quad (53)$$

The first term ($-\lambda_1 \ddot{\theta}_i$) represents fluid torque due to the added mass effect on the hull, and the remaining terms with the coefficients λ_2 and λ_3 represent the fluid torque due to the pressure drag between the opposite sides of the hull in the lateral (y) direction. Note that the effects of both linear and quadratic drag forces are considered. The parameters λ_1, λ_2 and λ_3 depend on the size and shape of the hull and are calculated for the general elliptical hull (Kelasidi, 2015) as shown below.

$$\lambda_1 = \frac{1}{12} \rho \pi C_M (a^2 - b^2)^2 L^3 \quad (54)$$

$$\lambda_2 = \frac{1}{6} \rho \pi C_f (a + b) L^3, \quad \lambda_3 = \frac{1}{8} \rho \pi C_f (a + b) L^4 \quad (55)$$

Note that C_M is the added mass torque coefficient, and the added mass term will be zero for the cylindrical hulls (as $a = b = r$), but it is a

non-zero value for the front and middle hulls due to the presence of thrusters. The action of fluid torque (τ_{fi}) and centrifugal force ($m_i R\omega^2$) to push the hulls outwards and the counteraction by joint torques (τ_{ij}) to maintain the joint angle are shown in Fig. 4(b) for a three-hull configuration vehicle. Note that there are N hulls with $N - 1$ joints, and the end joints at positions 1 and $N - 1$ will handle the net torque on the end hull and half on the following hull. The remaining inner joints denoted by ij th joint will handle half the torque requirement on both the i th hull and the j th hull. Hence, the corresponding torque requirement for each joint is calculated as shown below.

$$\tau_{12} = \frac{-(2\tau_{f1} + \tau_{f2}) + (2m_1 + m_2)R\omega^2 L}{2} \quad (56)$$

$$\tau_{(N-1)(N)} = \frac{-(2\tau_{fN} + \tau_{f(N-1)}) + (2m_N + m_{(N-1)})R\omega^2 L}{2} \quad (57)$$

$$\tau_{ij} = \frac{-(\tau_{fi} + \tau_{fj}) + (m_i + m_j)R\omega^2 L}{2} \quad (58)$$

Note that joint torque is significant for the split-hull vehicle as it determines whether the joints can hold the joint angles at a specific value. Let us go to the selection of the updated fluid coefficients next.

3.2.3. Estimation of the updated fluid coefficients

For the accuracy of the results, it is crucial to choose the hydrodynamic coefficients carefully. In this case, the steady-state flow in the transition region (Wiens and Nahon, 2012) is used, with a maximum speed of 0.5 m/s and a Reynolds number around 10^5 . Numerous studies have been done on the force acting on slender bodies under similar conditions. One of them was carried out by Kelasidi (2015), Gus'kova et al. (1998) and Khalil and Gallot (2007) and uses the drag coefficients $C_{d0} = 1$, $C_{f0} = 0.03$, and the added mass coefficients $C_{M0} = C_{a0} = 1$. However, she considered uniform, smooth cylinders, which is not the case here because of the discontinuities introduced by the servo joints. This problem needs to be solved by estimating the updated fluid coefficients that consider the effect of servo joints. To do that, a new parameter known as the discontinuity factor (d_{fx}), which is the ratio of net servo joint length ($l_j = 0.065$ m) to the effective length of the hull (L_e), is introduced. Fig. 5 shows the CAD design of a hull with the crucial dimensions indicated. The height of the joint is related to the length of the hull using another parameter denoted as d_{fz} . The servo joint is viewed as a thin rectangular block attached to the hull because of its low width ($w_j = 0.027$ m) in relation to its height ($h_j = 0.08$ m) as well as the effective length of the hull L_e . It should be noted that all hull configurations have equal dimensions for the joint section (l_j, h_j). In addition to these parameters, the ratio of the effective length (L_e) and the diameter ($2R$) of the hull is introduced as the effective slenderness of the hull (S_h). Given that both 1st and N th (exterior) hulls are connected only to a single servo joint, their d_{fx} values will be lower compared to the remaining (interior) hulls.

$$d_{fx} = \frac{l_j}{L_e}, \quad d_{fz} = \frac{h_j}{L_e}, \quad S_h = \frac{L_e}{D} \quad (59)$$

Let us first assess the revised added mass coefficients. It is necessary to account for the contributions from both cylindrical (hull) and rectangular (servo joint) parts when calculating the lateral added mass force (y direction). A thin rectangular block with dimensions of length $l_j/2$ and height h_j is subject to a lateral added mass force (Blevins, 1979), which is given as

$$f_{Aj} = \rho \pi \left(\frac{l_j^2}{16} \right) h_j \dot{v}_r. \quad (60)$$

Using Eq. (60) and merging it with Eq. (41) with the help of the parameters given in Eq. (59) gives the updated coefficients as shown in Eq. (61). Compared to the lateral counterpart and the mass of the hull, the thin rectangular and cylindrical parts have a negligible effect on

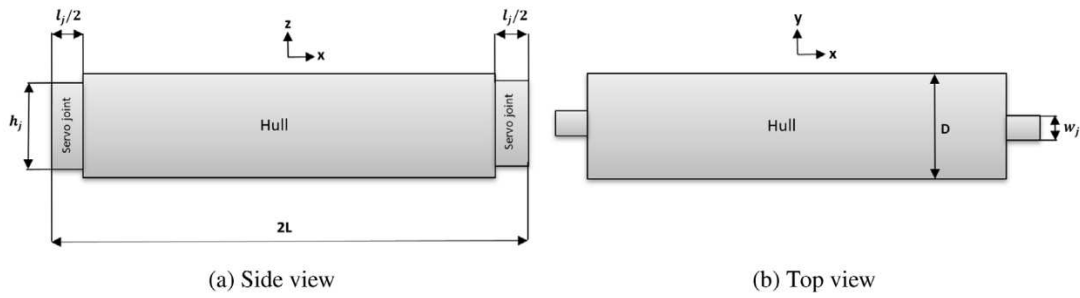


Fig. 5. CAD design showing the dimensions of an interior hull connected to servo joints on both ends.

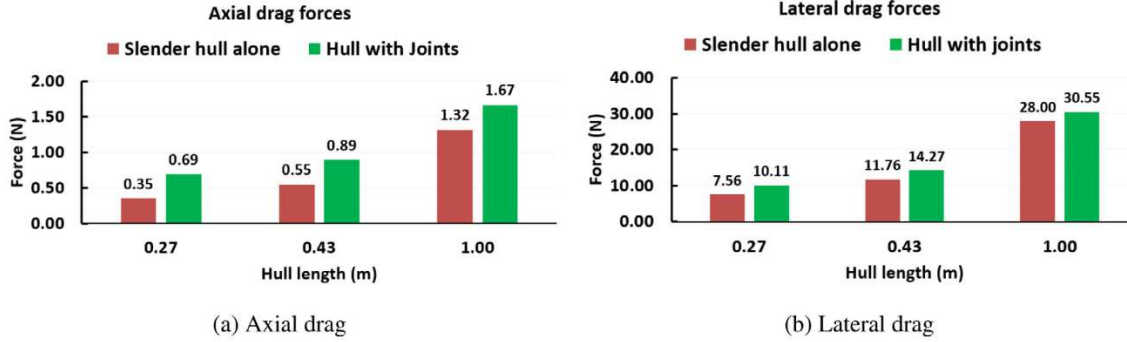


Fig. 6. Variation of the drag force for different hulls.

the axial added mass force (Blevins, 1979). Therefore, the axial added mass coefficients are disregarded in this paper.

$$C_a = C_{a0} \left(1 - d_{fx} + \frac{d_{fx}^2 S_h^2 d_{fz}}{2} \right) \quad (61)$$

Since the addition of the joints will impact both the axial and lateral drag coefficients (Blevins, 1979), they need to be updated. The lateral drag coefficients can be modified using analytical techniques similar to the added mass, but updating the axial drag component similarly with sufficient accuracy is beyond the scope of this paper. Hence, a simulation method using Ansys Fluent (Ansys Academic Research Fluent, 2015) is implemented for updating the drag coefficients. In that way, the general formula for the updated drag coefficients will be derived by considering three different hulls. Firstly, consider a hull with dimensions of $2L = 0.426$ m and $D = 0.1$ m, and the servo joints attached on both ends (see Fig. 5). Using the software (Ansys Academic Research Fluent, 2015), the fluid flow is simulated separately along the axial (x) and lateral (y) directions of the hull at 0.4 m/s. The corresponding drag force acting on the hull is measured in each case. These hull dimensions match the M-Hull vehicle available in the laboratory and will be used for the model validation in Section 5. Now, another hull is considered with the same overall dimensions ($2L, D$) but without the servo joints, and it is examined using the normal slender body theory. The same procedure is repeated for two more hulls with $2L = 1$ m and $2L = 0.27$ m having the same diameter ($D = 0.1$ m). These measurements represent the initial ($N = 3$) and final ($N = 11$) hull configurations for the proposed split-hull vehicle. The results of the drag simulation are shown in Fig. 6, and it is obvious that the drag force is increasing due to the presence of servo joints. This trend is expected because the joints disrupt the smooth cylindrical profile of the hull. From Fig. 6, it is clear that the hull length and the relative increase in the force value are inversely related. The relative impact of the servo joint, which has fixed dimensions, will be less noticeable the longer the hull. The axial drag force increases by a factor of 0.62 when $2L = 0.426$ m, 0.26 when $2L = 1$ m, and 0.98 when $2L = 0.27$ m. The best-fitting line, which is provided by (62), relates the change in axial drag force directly to d_f . It is interesting to note that the servo joints

have a lower effect on the lateral drag force; the fractional increase is 0.21 when $2L = 0.426$ m, 0.09 when $2L = 1$ m and 0.33 when $2L = 0.27$ m.

$$c_f = c_{f0}(1 + 4.01d_{fx}), \quad c_d = c_{d0}(1 + 1.4d_{fx}) \quad (62)$$

The following section explains the optimisation procedure for the suggested vehicle based on the modelling.

4. Analysis of the proposed vehicle

The optimisation process described below simulates the turning motion of various possible hull configurations (N) for the proposed split-hull vehicle. The optimal joint angle will vary depending on the vehicle configuration, and to determine it, simulations for each case must be performed separately, as described in Section 3. Based on this knowledge, the simulation is performed as follows.

4.1. Simulating different hull configurations of the proposed vehicle

The simulation is performed using (MATLAB, 2022), with the vehicle moving at a constant linear speed of 0.4 m/s while following a circular path with radius R . Below are the analysis findings for each hull configuration, along with Figs. 7, 8, 9 and 10 illustrate how various parameters can vary. Noting that Eqs. (4)–(19) are used to carry out the kinematic analysis first, the results are then applied to the dynamic modelling described in Section 3 to produce the desired results. Each step records the relevant parameters, such as the thrust requirement, turning diameter, and joint torque requirement. The outcomes are shown below. This procedure is repeated for each hull configuration by altering the value of N from three to eleven.

4.1.1. Three-hull configuration

Here, $N = 3$, $2L = 3/3 = 1$ m, and the base joint angle $\phi_0 = 60^\circ$ are the variables used. These values correspond to the Hexagonal turning mode; hence, the joint angles vary from 47.5° to 72.5° . As the joint angle increases, as shown in Fig. 7(a), the turning diameter drops from 2.27 m to 1.36 m. The difference is almost linear, and the diameter

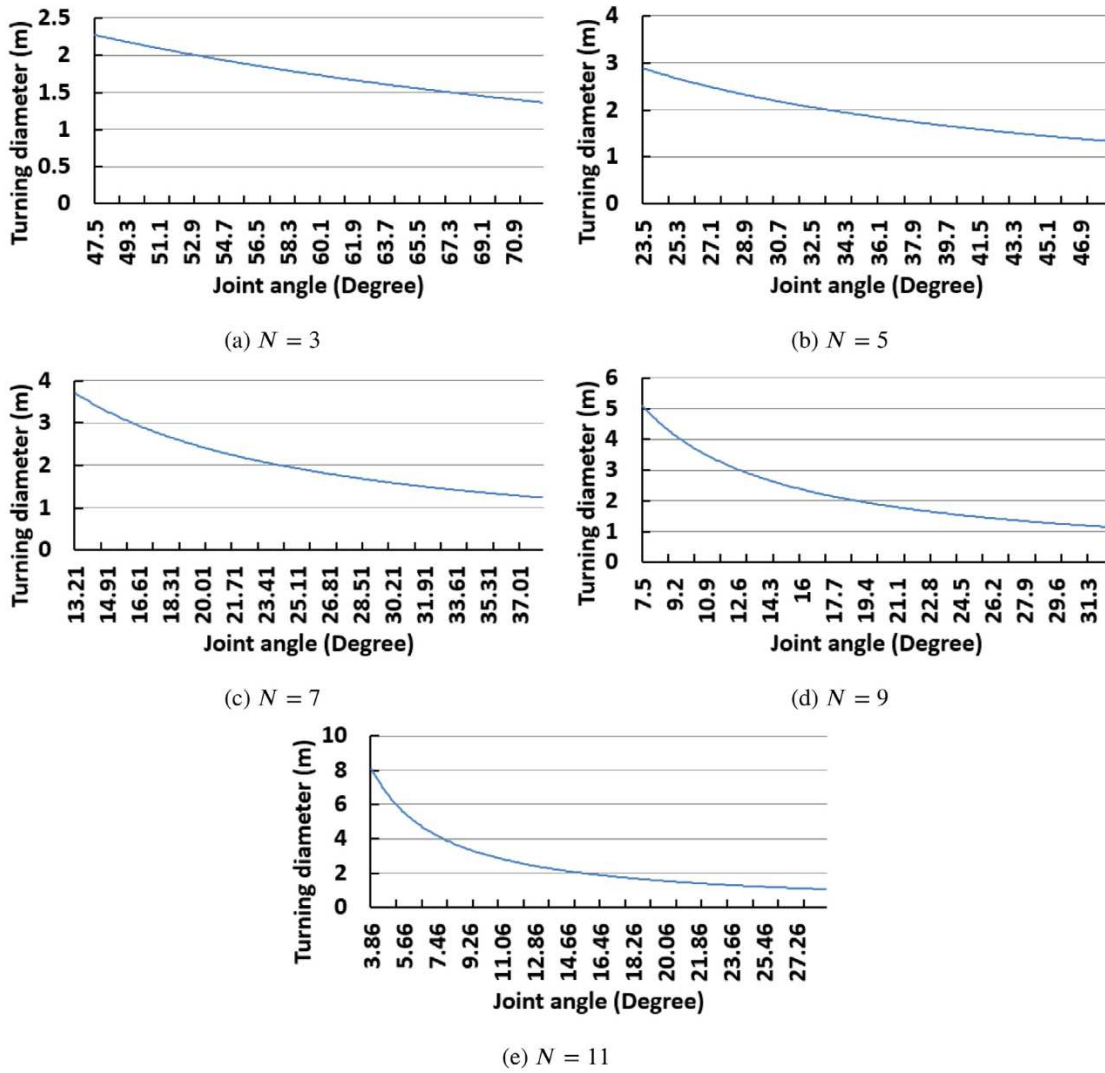


Fig. 7. Variation of the turning diameter corresponding to the different turning modes of each hull configuration (N).

never exceeds the vehicle length (3 m). Fig. 8(a) illustrates the linear increase in joint torque requirement from 2.7 N m to 4.39 N m. As shown in Fig. 9(a), lateral thrust gradually decreases with joint angle and only slightly increases at the very end, at about 70°. Higher joint angles favour lower lateral thrust requirements. In contrast, the axial thrust rises to reach a maximum value and then begins to decline gradually, although the change is much smaller than its lateral counterpart. Fig. 10(a) shows the variation of the thrust ratio (α_{xy}), which remains small for the majority of angles but suddenly increases to a value of 4022 for the joint angle of 71.2°. Although this angle seems advantageous for the analysis, a high joint torque must be considered.

4.1.2. Five-hull configuration

Here, $N = 5$, $2L = 3/5 = 0.6$ m, and the base joint angle $\phi_0 = 36^\circ$ are the key parameters. The joint angles range from 23.5° to 48.5°, and these values correspond to the Decagonal turning mode. As the joint angle increases, the turning diameter decreases from 2.88 m to 1.33 m, as shown in Fig. 7(b). The diameter is always smaller than the vehicle length, and the variation is almost linear. Fig. 8(b) illustrates the linear increase in joint torque requirement from 1.01 N m to 1.94 N m. According to the axial and lateral thrust variation in Fig. 9(b), lateral thrust initially decreases and then increases as a function of joint angle. On the other hand, the axial thrust rises to reach a maximum value and then begins to decline. The minimum lateral thrust point, in this case,

is less than the base joint angle (ϕ_0), in contrast to the previous case ($N = 3$). Fig. 10(b) shows a plot of the variation of the thrust ratio (α_{xy}), which remains small for the majority of angles but suddenly increases to a value of 1069 for the joint angle of 30.2°.

4.1.3. Seven-hull configuration

Here, the parameters are $N = 7$, $2L = 3/7 = 0.43$ m, and the base joint angle, ϕ_0 , is set to 25.71°. The joint angles range from 13.21° to 38.21°, and these values represent the Tetrakaidecagonal turning mode. As the joint angle increases, the turning diameter decreases from 3.69 m to 1.23 m, as shown in Fig. 7(c). This time, the variation is nonlinear; for the lower angles, the diameter is greater than the vehicle length. Fig. 8(c) illustrates the linear increase in joint torque requirement from 0.57 N m to 1.28 N m. The lateral thrust decreases first and then increases with the joint angle, according to the axial and lateral thrust variation shown in Fig. 9(c). The axial thrust rises initially, reaches a maximum value, and then begins to decrease, much like in earlier cases. However, the lateral thrust rises and reaches a value comparable to the axial thrust at higher joint angles. Additionally, compared to the five-hull configuration, the point of minimum lateral thrust arrives a little bit earlier. Fig. 10(c) shows the variation of the thrust ratio (α_{xy}), where it remains small for most angles but suddenly increases to a value of 1437 for the joint angle of 18.8°.

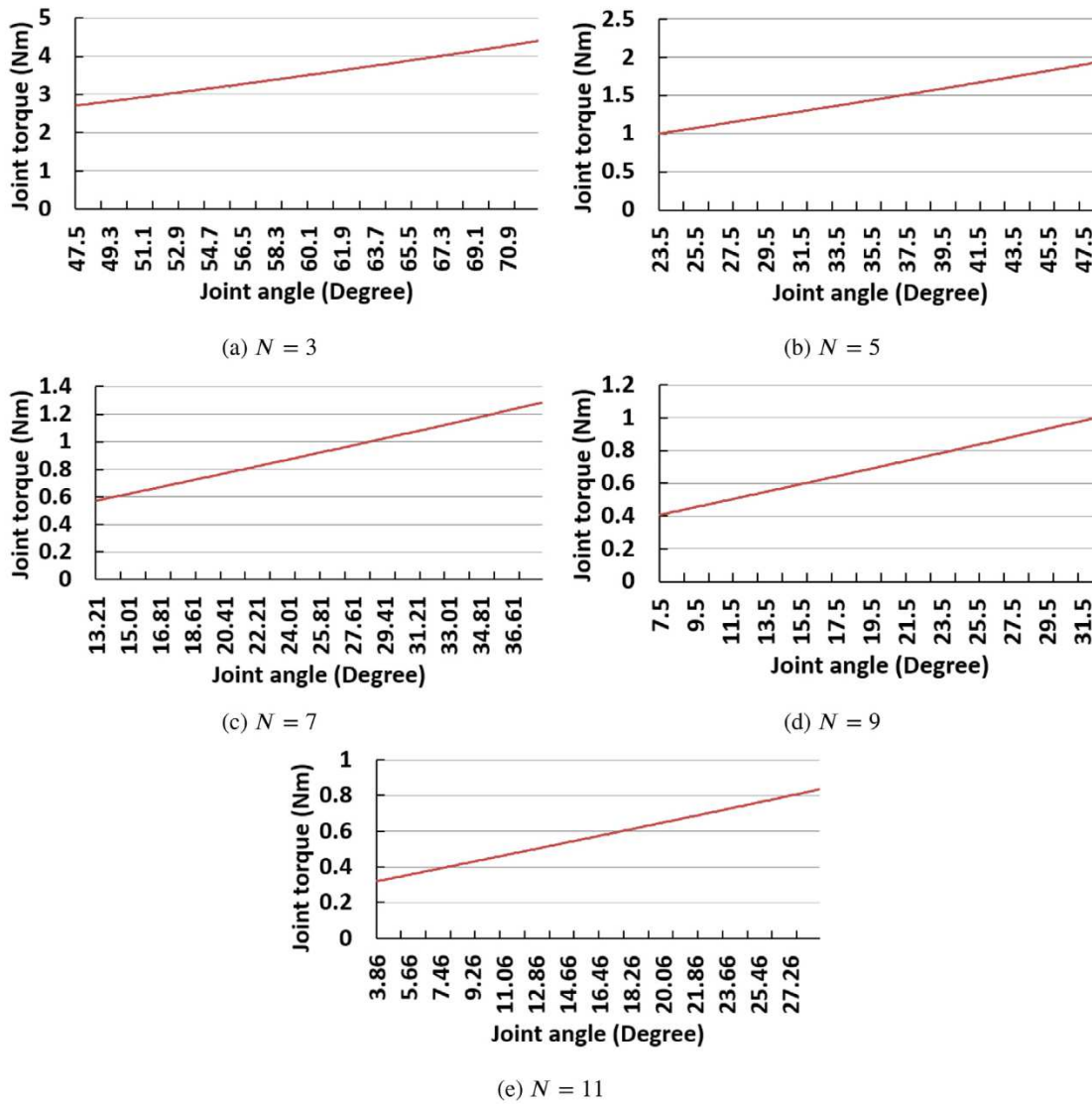


Fig. 8. Variation of the joint torque requirement for the different turning modes of each hull configuration (N).

4.1.4. Nine-hull configuration

$N = 9$, $2L = 3/9 = 0.33$ m are the parameters used in this case. The joint angles range from 7.5° to 32.5° , and $\phi_0 = 20^\circ$ represent the Octakaidecagonal turning mode. As the joint angle increases, the turning diameter decreases from 5.08 m to 1.14 m, as shown in Fig. 7(d). Similar to the previous instance, the variation is nonlinear this time, and the diameter is greater than the vehicle length for the initial angles. As shown in Fig. 8(d), the joint torque requirement rises linearly from 0.4 N m to 1.01 N m. According to the axial and lateral thrust variation in Fig. 9(d), lateral thrust initially decreases and then gradually increases with the joint angle. The axial thrust increases initially, reaches a maximum value, and then decreases, much like in earlier cases. It is interesting to note that the lateral thrust rises and even crosses the axial thrust at higher angles. Still, unlike in the previous instance, the point of minimum lateral thrust reaches a little later. Fig. 10(d) shows the variation of α_{xy} , which remains small for the majority of angles but suddenly increases to a value of 1598 for the joint angle of 13.5° .

4.1.5. Eleven-hull configuration

Here, the parameters are $N = 11$, $2L = 3/11 = 0.27$ m, and the base joint angle, ϕ_0 , is set to 16.36° . The joint angles range from 3.86° to 28.36° , and these values represent the Doicosagonal turning

mode. As the joint angle increases, the turning diameter decreases from 8.08 m to 1.05 m, as shown in Fig. 7(e). This time, the variation is very nonlinear; the diameter is greater than the vehicle length for most initial angles. Fig. 8(e) illustrates the linear increase in joint torque requirement from 0.32 N m to 0.83 N m. According to the axial and lateral thrust variation depicted in Fig. 9(e), the lateral thrust increases slightly at first, decreases to a minimum value, increases similarly to the previous cases, and decreases. Similar to the earlier cases, the axial thrust increases initially, reaches a maximum value, and decreases. It is interesting to note that, unlike prior cases, the lateral thrust crosses the axial one at higher joint angles. The point of minimal lateral thrust reaches even later than in the nine-hull configuration. Fig. 10(e) shows the variation of α_{xy} , where it remains small for most angles but suddenly increases to a value of 574 for the joint angle of 10.56° .

4.2. Comparison between the hull configurations

Figs. 11(a-d) compare the parameters corresponding to the optimal joint angle for each hull configuration (N) and plot the variations. When the equivalent turning mode as given in Fig. 11(a) is considered, the optimal turning angle is on the positive side for $N = 3$ and turns negative for all other configurations. It is negative with maximum magnitude at $N = 7$ and then loses its magnitude. When there are fewer

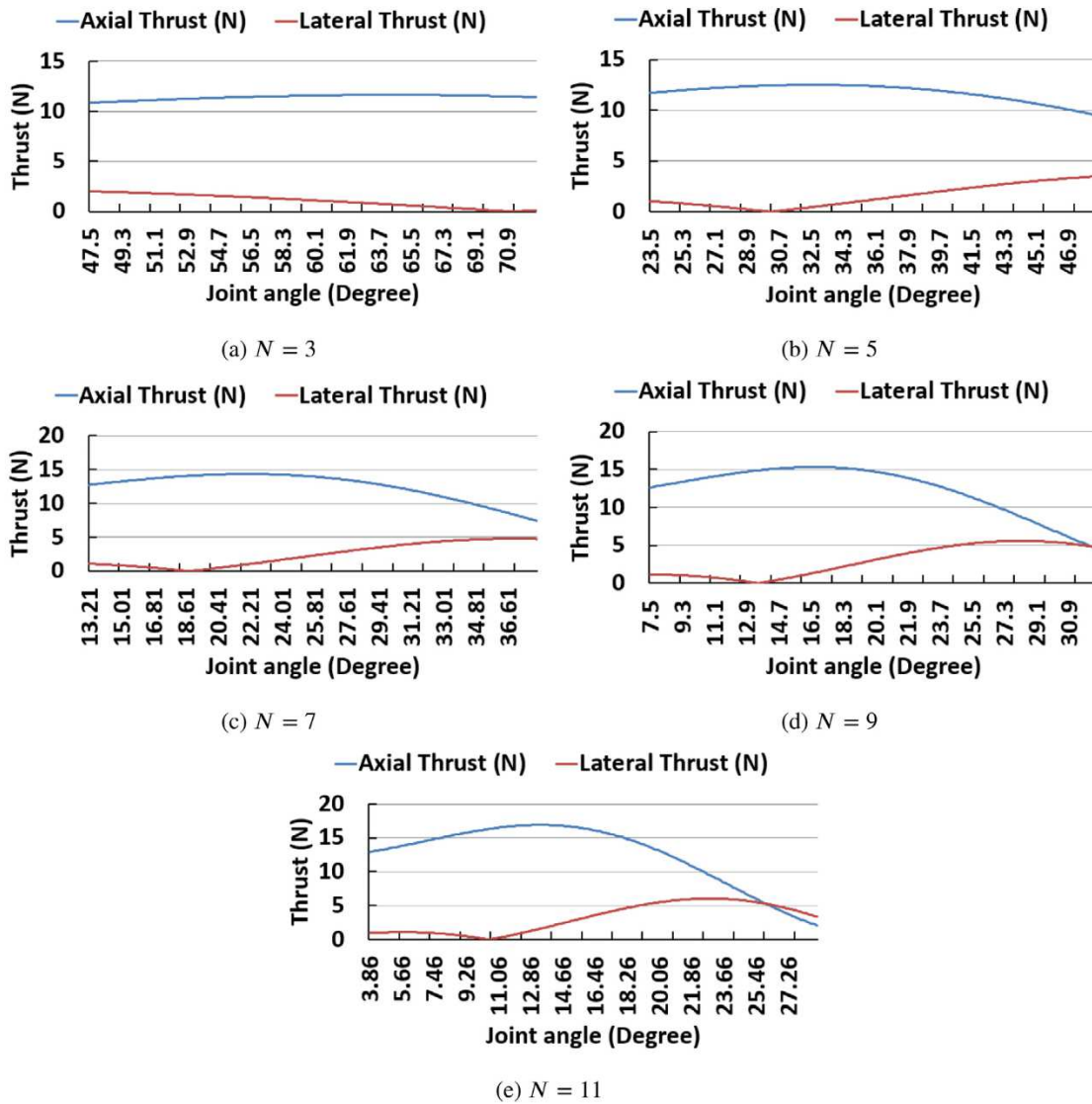


Fig. 9. Variation of the thrust requirement for the different turning modes of each hull configuration (N).

hulls, the optimal turning angle is higher than the base value; conversely, it is lower when there are more hulls. According to Fig. 11(b), the turning diameter increases continuously as the number of hulls (N) increases, but the rate of increase drops for higher values of N . When there are more than eleven hulls, the body length exceeds 3 m, showing a disadvantage of having an excessive number of hulls. Moreover, the joint torque is inversely related to the number of hulls. Fig. 11(c) illustrates that the torque needed for the three-hull configuration is much higher at 4.29 N m than for the eleven-hull configuration at 0.45 N m. The thrust ratio (α_{xy}), which is shown in Fig. 11(d), is highest for a smaller hull configuration. Interestingly, the ratios are still in three-digit numbers for higher hull configurations, as it is 574 for $N = 11$. A non-dimensional parameter (H) is defined to select the best configuration that takes all of these considerations into account as

$$H = c_{xy} \frac{\alpha_{xy}}{1000} + c_R \frac{l}{2R} + c_\tau \frac{\tau_{max} - \tau}{\tau_{max}}. \quad (63)$$

Here, c_{xy} , c_R and c_τ are the coefficients for the Thrust ratio (α_{xy}), Turning diameter ($2R$) and Joint torque (τ_{ij}) terms, respectively. Note that τ_{max} is the torque capacity of the servo joints, which according to the vehicle design, is 4.5 N m, and l is the vehicle length. τ is the joint torque requirement, and $2R$ is the turning diameter necessary to meet the minimum lateral thrust condition. The coefficients can

be configured to suit specific design needs, and the objective is to achieve the highest thrust ratio (α_{xy}) with the lowest turning diameter. The joint torque is comparatively less important because the proposed servo joints can deliver enough torque even in the worst-case scenario. For example, $\tau = 4.29$ N m for the three-hull configuration vehicle. Therefore, the coefficients are chosen as $c_{xy} = 1.5$, $c_R = 1$ and $c_\tau = 1$ to focus on the lateral thrust optimisation factor in this paper. According to equation Eq. (63), the value of H is determined, and Fig. 12 shows its variation. The value of H ranges from 2.78 for the eleven-hull configuration to 8.23 for the three-hull configuration. It is important to consider that the outcome will vary depending on the design priority. If the focus were on minimising the joint torque, a higher coefficient c_τ must be used, and the outcomes would be different. Since the servo motors have enough capacity as per the design, a vehicle with a lower hull configuration will meet the needs better than one with a higher one.

5. Model validation

M-Hull, the prototype split-hull underwater vehicle created in the laboratory and previously used for various studies (Kumar and Rajagopal, 2019, 2021), was used to test the accuracy of the analysis in a

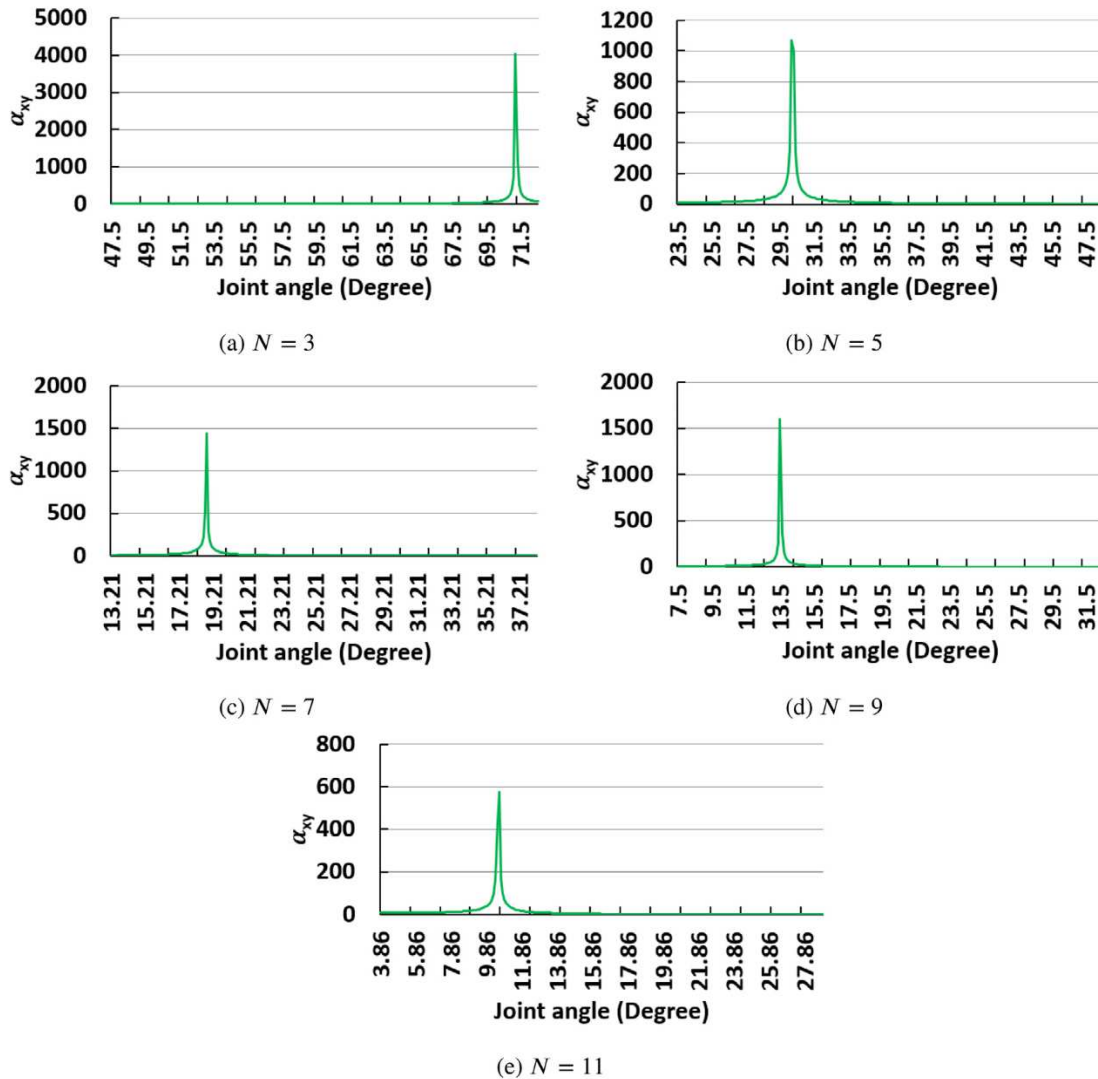


Fig. 10. Variation of the Thrust ratio for the different turning modes of each hull configuration (N).

real-world scenario. It has a similar configuration to the proposed split-hull vehicle, but the total length is 1.28 m with three hulls. However, it satisfies all the criteria outlined in Section 2 for using the modelling approach suggested in this paper. As the vehicle does not have sway thrusters, any significant lateral thrust requirement (f_{tN_y}) indicates a net unbalanced force in the same direction, meaning the motion is impossible without the vehicle slipping. Also, the lack of thrust prevents reaching the desired turning speed. First, the normal turning modes are analysed before estimating the optimal one, and then the model is experimentally validated.

5.1. Normal turning modes of M-Hull

The joint angles listed in Table 2 are used to define and analyse the specific turning modes (n) of the vehicle. Before the concept of optimal turning mode was introduced, these were the normal turning modes used for the vehicle. Hence it is interesting to find out the penalty for not choosing the optimal one in each case. Fig. 3(a) depicts the schematic representation of the vehicle travelling along a circular path in a hexagonal configuration ($n = 6$). First, the lateral thrust variation with the normal turning modes is analysed. The joint angles ϕ_{12} and ϕ_{23} are chosen in accordance with the turning mode (n) listed in Table 2, and the parameters are $N = 3$, $2L = 0.426$ m, turning speed (u) = 0.4 m/s. The procedure outlined in Section 3.2.3 is used

to update the fluid coefficients for the vehicle. The rear hull does not have a thruster attached, as shown in Fig. 2, while the front and middle hulls both have them. Additionally, only one servo joint connects the front and rear hulls to the middle hull, which has two. As a result, the fluid coefficients for each hull vary, and the calculations are performed as described in Section 3. According to Eq. (52), the variation in thrust requirements for each mode is calculated, and the results are displayed in Fig. 13(a). For all turning modes, it is evident that the lateral thrust (f_{tN_y}) is significant relative to the axial thrust (f_{tN_x}), but it is very low between $n = 5$ and $n = 7$. It implies that better turning modes may exist within the same range and that using the proper turning mode can reduce the net lateral thrust requirement. Instead of being limited by the values in Table 2, it is crucial to conduct a thorough analysis of the vehicle, considering all possible joint angles to determine that. In doing so, the optimal joint angle can be estimated, and the net lateral forces on the vehicle can be decreased.

5.2. Finding the optimal turning mode for M-Hull

Fig. 13(a) clarifies that the ideal joint angle will fall between $n = 5$ and $n = 7$ modes because the lateral thrust is at its lowest in this range. The corresponding joint angles are, respectively, 72° and 51.43° . Let us begin with the vehicle simulation, which is carried out as described in Section 3, with the parameters $N = 3$, $2L = 0.426$ m, $D = 0.1$ m,

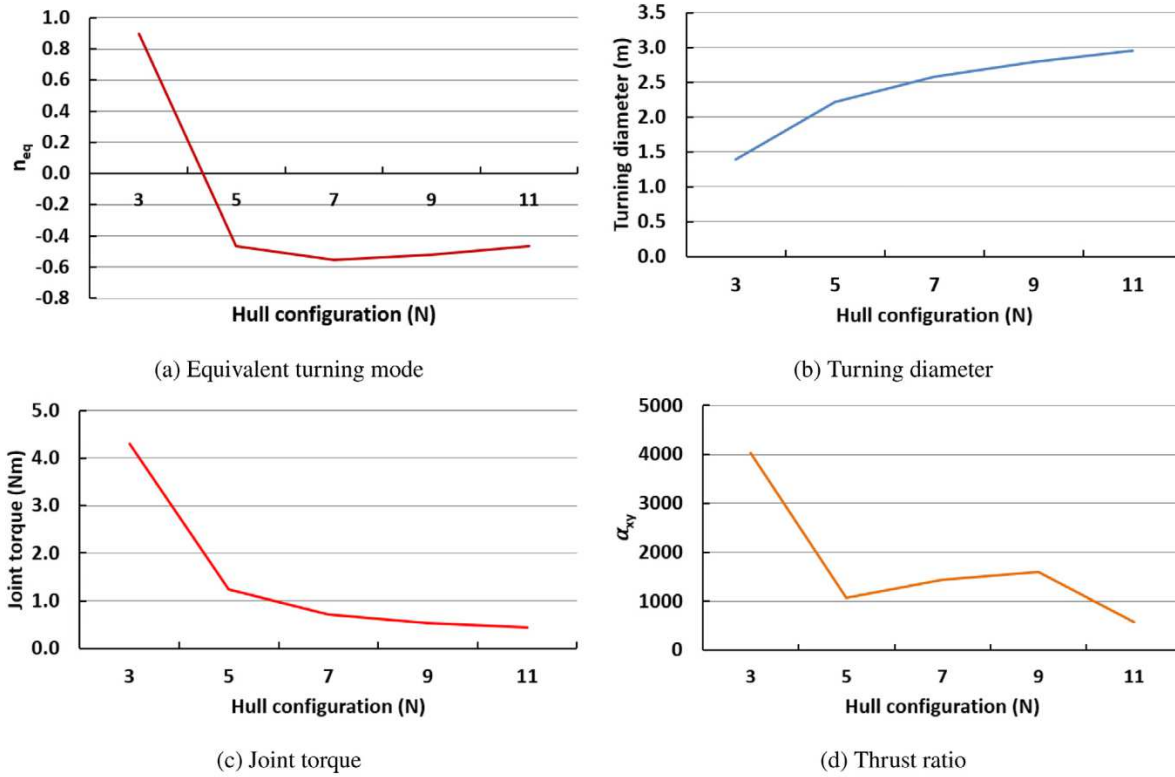


Fig. 11. Variation of different parameters with respect to the hull configuration (N), measured at minimum lateral thrust condition.

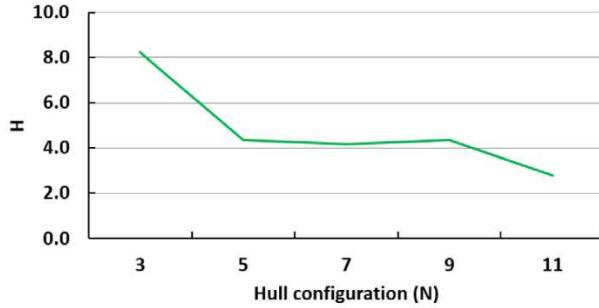


Fig. 12. Schematic diagram comparing the optimisation parameter (H) for different turning modes (N).

Table 2
Joint angle for each turning mode.

Turning mode	Mode name	Joint angle (deg)
5	Pentagonal	72
6	Hexagonal	60
7	Heptagonal	51.43
8	Octagonal	45
9	Nonagonal	40
10	Decagonal	36

$u = 0.4$ m/s, and base joint angle $\phi_0 = 60^\circ$ as per Eq. (1). Similar to the three-hull configuration vehicle described in Section 4, it corresponds to the hexagonal turning mode. The joint angles range from 47.5° to 72.5° . The vehicle is simulated to follow a circular path at each joint angle, similar to the proposed vehicle described in Section 4. The corresponding thrust ratio values are determined using Eq. (2). In each scenario, the required joint torque (τ_{ij}) and turning diameter ($2R$) are also estimated. Fig. 13(b) illustrates how the thrust ratio varies with joint angle. The vehicle has a maximum thrust ratio of 1867 at a joint

angle of 62.7° . The next step is the experimental validation of the model, which is described as follows.

5.3. Validating the model using M-Hull

To validate the model presented in this paper and to check the difference between normal and optimal turning modes, the performance of M-Hull is experimentally evaluated. The photographs of the vehicle during the experiments are shown in Fig. 14. The conditions are similar to the modelling used in this paper, including $u = 0.4$ m/s and the joint angles are varied to obtain different turning modes (n). The operating depth is 0.2 m to ensure the vehicle is completely submerged. It should be noted that if the thrusters do not deliver the necessary axial and lateral thrust, the vehicle will not be able to cover the desired path. Angles of 72° , 67° , 60° , 51.43° , 45° and the estimated optimal joint angle of 62.7° are used for the experiment. The vehicle is commanded to cover the circular path using these joint angles where the thruster signals are generated (Blue Robotics, 2020) according to the axial thrust value obtained in Section 3. A vertical camera system is used in each case to measure the actual turning diameter ($2R_{act}$) and speed (u_{act}) (Kumar and Rajagopal, 2021). The parameters are listed in Table 3, and it is obvious that all non-optimal modes have thrust ratios (16) much lower than the optimal one (1867), which corresponds to the joint angle of 62.7° . The measured turning diameters ($2R_{act}$) for all non-optimal turning modes are higher than the estimated one ($2R$) because of the vehicle slipping, and the turning speeds (u_{act}) are much lower because of the insufficient thrust. The error values in turning speed and diameter are critical in turning motion and are shown in Fig. 15. For the optimal turning mode, the error values are under 2%. The figure also shows that the error continues to grow as the thrust ratio decreases. A notable point is the hexagonal mode ($\phi = 60^\circ$), where the error values are very less compared to other non-optimal modes. Due to its proximity to the optimal turning mode, the thrust ratio is relatively higher (15.84). The thrust ratio graph in Fig. 13(b), which shows that α_{xy} is high (>10) for a range of joint angles from 59.5° to

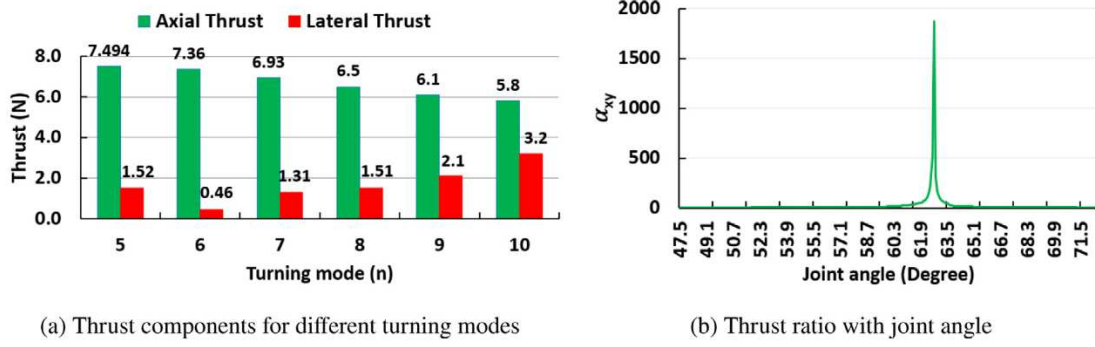


Fig. 13. Variation of the thrust components and thrust ratio for M-Hull.

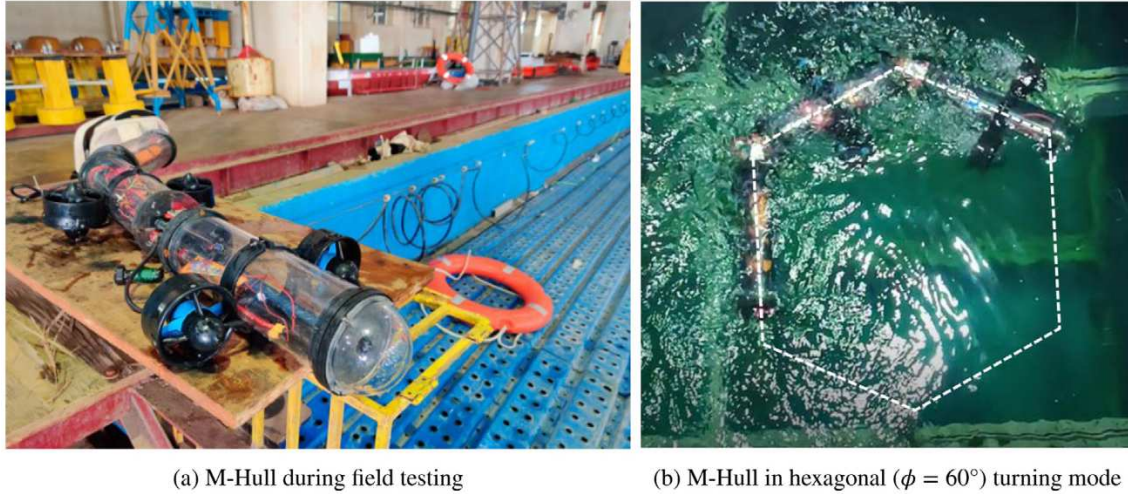


Fig. 14. Pictures of the three-hull vehicle (M-Hull) during the experiments.

Table 3

Comparison of turning modes in terms of thrust, joint torque requirements and turning diameter at $u = 0.4$ m/s.

ϕ_{ij} (deg)	τ_{ij} (N m)	f_{IN} (N)	α_{xy}	$2R$ (m)	$2R_{act}$ (m)	u_{act} (m/s)
45	0.813	6.519	4.3	1.030	1.2	0.326
51.43	0.946	6.935	5.3	0.886	0.98	0.348
60	1.108	7.362	15.84	0.740	0.76	0.394
62.7	1.12	7.382	1867	0.7	0.71	0.396
67	1.26	7.42	9.2	0.64	0.67	0.378
72	1.427	7.494	4.92	0.587	0.65	0.345

65°, also makes this point. It suggests that even if the joint angle is slightly different, the vehicle will still turn nearly optimally. In such cases, the lateral thrust requirement is low to make a significant error in the turning speed and diameter. Thus the experimental results align with the modelling-simulation results for the split-hull vehicle.

6. Conclusions

The kinematics and dynamics of the 2D turning motion of an under-actuated serial split-hull underwater vehicle with elliptical/circular cross-section hulls have been modelled. The split-hull design increases the manoeuvrability and the operation efficiency of the vehicle compared to the single hull version. Turning motion is a critical aspect of any underwater vehicle due to the lateral action of the Coriolis-centrifugal forces. Generally, any underwater vehicle needs the combined action of both surge and sway thrusters to follow the circular path. During the turning motion, the differential orientation of the hulls in a split-hull underwater vehicle pointed the way to minimise this net

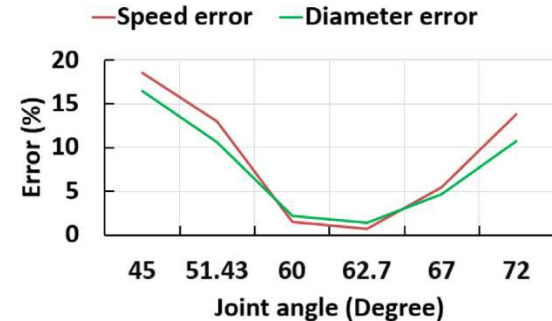


Fig. 15. Variation of the error values with joint angle for M-Hull.

lateral force without using the sway thrusters. Hence, with the help of a detailed simulation-based analysis and experimental results, it is proved that the split-hull vehicle can significantly minimise the lateral thrust requirement if a proper turning mode is selected. The turning performance of various hull configurations of the vehicle in terms of the factors including thrust ratio (α_{xy}), joint torque requirement (τ_{ij}) and turning diameter ($2R$) are compared. It is possible to minimise the lateral thrust requirement in any hull configuration (N) to a negligible value if proper turning mode (n) is selected. Note that the net effect of forces and the lateral thrust never becomes zero as all the hulls are not identical, but it will have almost zero impact on the vehicle compared to the non-optimal turning modes. A higher number of hulls results in a reduced joint torque requirement, higher turning diameter, and a lower thrust ratio. The optimal turning diameter for the eleven

hull configuration is higher than the vehicle length (l), which is against the fundamental purpose of splitting the hull: lowering the turning diameter and increasing the manoeuvrability. At the same time, a smaller hull configuration (N) results in a better turning operation due to its lower turning diameter ($2R$) and higher thrust ratio (α_{xy}). However, there is a drawback with a high joint torque requirement which demands powerful servo joints. A dimensionless parameter (H) is defined to compare various hull configurations to make conditional decisions. Suppose the servo motors can produce sufficient torque. In that case, it is recommended to go for a smaller number of hulls to achieve a minimum-lateral force condition and a smaller turning diameter. If the servo motors are weak, it is better to consider a higher number of hulls at the expense of higher turning diameter and lateral forces. The experimental results prove that these results are valid in the real-world scenario with error values below 5%. The critical point is that the drag-added mass coefficients must be calculated with sufficient accuracy, as explained in Section 3.2.3. The vehicle has a few additional components, such as wires and connectors in the actual scenario. The accuracy of the thruster output and minor irregularities on the hull surface are also ignored in the simulation stage. Still, the effects are minor, visible from the negligible error in results corresponding to the optimal turning mode. It is also found that the vehicle operates in a near-optimal turning mode for a range of joint angles instead of a specific value. It is clear from Fig. 15 that the error values for non-optimal turning modes are very high. It is due to the added effect of both the hull slipping and the resulting lateral velocity (v) that violates the basic assumptions described in Section 2. Note that these results are based on the specific design of the vehicle and will vary according to the hull shape, thruster position and presence of additional components. However, the method followed here can be used with a few modifications to get the results for similar vehicles.

7. Future works

The focus of this paper was on improving the turning performance by placing more emphasis on the turning diameter and lateral thrust requirement than on the joint torque. If necessary, more significant consideration can be given to the joint torque and research on it similarly. Additionally, in this research, the focus was on the hulls with cylindrical and elliptical cross-sections. The modelling of hulls with different shapes will be exciting and inspire more work in the future. This research was conducted on the vehicle without considering how the number of hulls would impact the complexity of the fabrication process. Additionally, this research ignores any potential increase in the power consumption brought on by increasing the number of servo joints. It results in an extended optimisation problem taking these variables into account.

CRediT authorship contribution statement

Vishakh S. Kumar: Conceptualization, Resources, Software, Validation, Writing – original draft. **Prabhu Rajagopal:** Methodology, Project administration, Funding acquisition, Writing – review & editing.

Declaration of competing interest

The authors declare that they have no known competing financial interests or personal relationships that could have appeared to influence the work reported in this paper.

Data availability

No data was used for the research described in the article.

Acknowledgements

The first author would like to thank M. Karthikeyan and Siddharth Shankar from the Mechanical Department, IIT Madras, India, for their support. The authors gratefully acknowledge the Department of Ocean Engineering, IIT Madras and the National Technology Centre for Ports, Coasts and Waterways for this project.

References

- Allen, Ben, Stokey, Roger, Austin, Tom, 1997. REMUS: a small, low cost AUV; system description, field trials and performance results. In: Oceans 1997. MTS/IEEE Conference Proceedings, Nova Scotia, Canada, Vol. 2. IEEE, pp. 994–1000.
- Ansys Academic Research Fluent, 2015. Version 16.2. Ansys Inc., Canonsburg, Pennsylvania.
- Blevins, Robert D., 1979. Formulas for Natural Frequency and Mode Shape. Van Nostrand Reinhold Co., New York, pp. 386–418.
- Blue Robotics, 2020. Blue robotics T100. [Accessed on 19-06-2020], (A Website).
- Borlaug, I.L.G., Gravdahl, J.T., 2019. Trajectory tracking for underwater swimming manipulators using a super twisting algorithm. *Asian J. Control* 21 (1), 208–223.
- Borlaug, I.L.G., Sverdrup-Thygeson, J., Pettersen, K.Y., Gravdahl, J.T., 2019. Combined kinematic and dynamic control of an underwater swimming manipulator. In: 12th IFAC Conference on Control Applications in Marine Systems, Robotics, and Vehicles CAMS, Daejeon, South Korea, Vol. 52. pp. 8–13, (21).
- Boyer, Frédéric, Porez, Mathieu, Khalil, Wisama, 2006. Macro-continuous computed torque algorithm for a three-dimensional eel-like robot. *IEEE Trans. Robot.* 22 (4), 763–775.
- Chen, Weishan, Xia, Dan, Liu, Junkao, 2008. Modular design and realization of a torpedo-shape robot fish. In: Proceedings of 2008 IEEE International Conference on Mechatronics and Automation, ICMA 2008, Takamatsu, Japan. pp. 125–130.
- Cox, R.G., 1970. The motion of long slender bodies in a viscous fluid. Part 1. General theory. *J. Fluid Mech.* 44, 791–810.
- Crespi, A., Ijspeert, A.J., 2006. Amphibot II : An amphibious snake robot that crawls and swims using a central pattern generator. In: Conference on Climbing and Walking Robots, London, UK. pp. 19–27.
- Cruz, Nuno A., Matos, Anibal C., 2008. The MARES AUV, a modular autonomous robot for environment sampling. In: OCEANS 2008, Quebec City, QC, Canada. IEEE, pp. 1–6.
- Dharwada, Srikanth, Agarwal, Aman, Rajagopal, Prabhu, 2018. Comparison of bio-inspired flapping foil propulsion systems with rotary propulsion. In: Bioinspiration, Biomimetics, and Bioreplication VIII, Vol. 10593. International Society for Optics and Photonics, pp. 194–201.
- Dharwada, Srikanth, Ravichandran, Santhosh, Rajagopal, Prabhu, Hingole, Vishal, 2019. Numerical study on swimming performance based on flapping orientations of caudal fins for bio-robotic systems. In: Proceedings of the Advances in Robotics 2019, Chennai, India. pp. 1–11.
- Gus'kova, N.Yu., Makhortykh, G.V., Shcheglova, M.G., 1998. Inertia and drag of elliptic cylinders oscillating in a fluid. *Fluid Dyn.* 33 (1), 91–95.
- Hirata, Koichi, Takimoto, Tadanori, Tamura, Kenkichi, 2000. Study on turning performance of a fish robot. In: International Symposium on Aqua Bio-Mechanisms, Hawaii, USA. pp. 287–292.
- Hoffmann, Bjørn Håvard, 2018. Path Following and Collision Avoidance for an Underwater Swimming Manipulator (Master's thesis). Norwegian University of Science and Technology (NTNU), Trondheim, Norway.
- Kelasidi, E., 2015. Modeling, Control and Energy Efficiency of Underwater Snake Robots (Ph.D. thesis). Norwegian University of Science and Technology (NTNU), Trondheim, Norway, p. 261.
- Kelasidi, E., Liljeback, Pal, 2016. Innovation in underwater robots: Biologically inspired swimming snake robots. *IEEE Robot. Autom. Mag.* 23 (1), 44–62.
- Kelasidi, E., Pettersen, K.Y., Gravdahl, J.T., 2015. Energy efficiency of underwater robots. In: IFAC Conference on Manoeuvring and Control of Marine Craft MCMC 2015, Vol. 48. pp. 152–159, (16).
- Kelasidi, E., Pettersen, K.Y., Gravdahl, J.T., 2017. Modeling and propulsion methods of underwater snake robots. In: 2017 IEEE Conference on Control Technology and Applications (CCTA), Hawaii , USA. IEEE, pp. 819–826.
- Kelasidi, E., Pettersen, K.Y., Liljeback, P., 2016. Locomotion efficiency of underwater snake robots with thrusters. In: SSRR 2016 - International Symposium on Safety, Security and Rescue Robotics, Lausanne, Switzerland. pp. 174–181.
- Keller, Joseph B., Rubinow, Sol, 1976. Slender-body theory for slow viscous flow. *J. Fluid Mech.* 75 (4), 705–714.
- Khalil, Wisama, Gallot, Guillaume, 2007. Dynamic modeling and simulation of a 3-D serial eel-like robot. *IEEE Trans. Syst. Man Cybern. C* 37 (6), 1259–1268.
- Krishnadas, Arun, Ravichandran, Santhosh, Rajagopal, Prabhu, 2018. Analysis of biomimetic caudal fin shapes for optimal propulsive efficiency. *Ocean Eng.* 153, 132–142.
- Kumar, Vishakh S., Rajagopal, Prabhu, 2019. Development and analysis of an autonomous underwater inspection vehicle with enhanced maneuverability. In: OCEANS 2019 - Marseille. pp. 1–8.

- Kumar, Vishakh S., Rajagopal, Prabhu, 2021. Modelling and analysis of turning motion of a subsurface mapping AUV with split-hull design. *J. Mar. Sci. Appl.* 20 (2), 284–301.
- Lighthill, Michael James, 1971. Large-amplitude elongated-body theory of fish locomotion. *Proc. R. Soc. B* 179 (1055), 125–138.
- Liljeback, Pal, Mills, Richard, 2017. Eelume: A flexible and subsea resident IMR vehicle. In: OCEANS 2017, Aberdeen, Vol. 2017-Octob. pp. 1–4.
- MATLAB, 2022. Version 9.12.0 (R2022a). The MathWorks Inc., Natick, Massachusetts.
- Miles, R.E., 1964. Random polygons determined by random lines in a plane. *Proc. Natl. Acad. Sci. USA* 52 (4), 901.
- Morison, J.R., Johnson, J.W., Schaaf, S.A., 1950. The force exerted by surface waves on piles. *J. Pet. Technol.* 2 (05), 149–154.
- Newman, J.N. (John Nicholas), Grue, John, 1977. Marine hydrodynamics. The MIT Press, Cambridge, UK, p. 426.
- Prester, Timothy, 2001. Verification of a Six-Degree of Freedom Simulation Model for the REMUS100 AUV (Master's thesis). Massachusetts Institute of Technology, Cambridge, MA 02139, United States.
- Severholt, Josefine, 2017. Generic 6-DOF Added Mass Formulation for Arbitrary Underwater Vehicles based on Existing Semi-Empirical Methods (Master's thesis). KTH, Naval Systems, p. 51.
- Sverdrup-Thygeson, J., Kelasidi, E., 2017. The underwater swimming manipulator—A bioinspired solution for subsea operations. *IEEE J. Ocean. Eng.* 43 (2), 402–417.
- Sverdrup-Thygeson, J., Kelasidi, E., Pettersen, K.Y., Gravdahl, J.T., 2016. Modeling of underwater swimming manipulators. *IFAC-PapersOnLine* 49 (23), 81–88.
- Wiens, A.J., Nahon, M., 2012. Optimally efficient swimming in hyper-redundant mechanisms: control, design, and energy recovery. *Bioinspir. Biomim.* 7 (4), 046016.
- Yu, Junzhi, Wang, Long, 2007. Geometric optimization of relative link lengths for biomimetic robotic fish. *IEEE Trans. Robot.* 23 (2), 382–386.
- Zhang, Chao, Hedrick, Tyson L., Mittal, Rajat, 2015. Centripetal acceleration reaction: an effective and robust mechanism for flapping flight in insects. *PLoS One* 10 (8), e0132093.
- Zuo, Zhijian, Wang, Zhifeng, 2008. Serpentine locomotion of a snake-like robot in water environment. In: 2008 IEEE International Conference on Robotics and Biomimetics, ROBIO, Bangkok, Thailand. pp. 25–30.